



國立臺灣大學電機資訊學院光電工程學研究所

碩士論文

Graduate Institute of Photonics and Optoelectronics
College of Electrical Engineering and Computer Science
National Taiwan University
Master Thesis

以兩步驟磊晶硒化鉍薄膜之磁運輸探討

Investigating Magnetotransport Properties of Two-Step
Epi-growing Bi_2Se_3 Thin Films

黃家均

Chia-Chun Huang

指導教授：黃建璋 博士

Advisor: Jian-Jang Huang, Ph.D.

中華民國 112 年 7 月

July 2023

國立臺灣大學碩士學位論文
口試委員會審定書



MASTER'S THESIS ACCEPTANCE CERTIFICATE
NATIONAL TAIWAN UNIVERSITY

以兩步驟磊晶硒化鉍薄膜之磁運輸探討

Investigating Magnetotransport Properties of Two-Step
Epi-growing Bi_2Se_3 Thin Films

本論文係黃家均君（學號 R10941065）在國立臺灣大學光電工程學研究所完成之碩士學位論文，於民國 112 年 7 月 27 日承下列考試委員審查通過及口試及格，特此證明

The undersigned, appointed by the Graduate Institute of Photonics and Optoelectronics, on 27 July 2023 have examined a Master's thesis entitled above presented by CHIA-CHUN HUANG (student ID:R10941065) candidate and hereby certify that it is worthy of acceptance.

口試委員 Oral examination committee:

(指導教授 Advisor)

黃建璋

林晏如

吳育仁

吳通奇

吳肇欣

所長 Director:

吳育仁

致謝



韶光荏苒，轉瞬已接近碩士生涯的下旬了。在台灣大學光電工程所中獲得了許多未曾想像過的寶貴經驗。從剛踏入這個陌生的環境，經過了兩年的淬鍊，在這裡收穫了滿滿滿從老師到同儕們的幫助。首先我要特別感謝我的指導教授黃建璋老師，不論從收集資料到實踐於實驗上，都給予滿滿的資源及幫助，在一籌莫展之際，都能及時給予適當的方向來順利進行，並且耐心地討論實驗細節與結果，並敦促我有更積極的表現。

碩士生涯能過順利完成，要感謝好多人，首先我非常謝謝育資學姊在碩一帶領我學會好多實驗所需的技能，不厭其煩地面對及回答我的疑惑，在我面臨困境時不時伸出溫暖的手給予我建議，也非常感謝岱頡學長陪伴幫助我一起完成實驗需要的架構，謝謝 Anuj 學長在我面臨擬合困境時，仍願意利用自己閒暇的時間幫我一起想辦法，謝謝亮昀、泓毅跟昱全在我無所適從不知該如何是好的時候，花時間與我聊聊，給我溫暖及鼓勵，讓我能夠在碩士生涯繼續往前走，謝謝學弟丞毅不遺餘力的與我討論我研究上的困難。謝謝泳辰及旻珊在實驗上的幫忙，因為有你們，HBT 計畫而順利走下去，也謝謝 Rohit 學長、志綱學長、晨瑋、浩方、宇翔、遠超、思安，因為你們，在實驗室裡能激盪出許多不一樣的想法及火花，而實驗室才可以順利地運轉，非常感謝實驗室的大家！

在碩論的尾聲能夠順利完成還要特別感謝成大的李民楷先生及鏘線的陳德昌先生，能夠給予全力的支持與協助，讓最後的量測順利圓滿，滿滿的感謝溢於言表。

另外我要最感謝我的家人爸爸媽媽哥哥跟阿嬤，他們從不過問及干涉我研究生涯的任何規劃，只會給予滿滿的精神支持，不論遇到什麼困難會聽我傾訴，再鼓勵我在研究這條路上繼續往下走。也要感謝我的國中高中大學各路朋友們，謝謝在無數個墜落的時刻接住我，也謝謝我的男朋友為我的研究生涯增添許多色彩，讓台北的日子變得難能可貴而有趣。



摘要

近年來，凝聚態物理學和材料科學領域對拓撲絕緣體表現出了極大的興趣，這是因為它們預測的獨特物理性質以及在自旋電子學和量子計算中的潛在應用。拓撲絕緣體是一類材料，其塊材 (bulk) 帶隙並呈現絕緣體特性，同時在表面存在導電的拓撲表面態，這些表面態由時間反演對稱性所保護。在這項研究中，我們選擇了三維拓撲絕緣體的硒化鉍作為我們的靶材。我們比較了沉積在藍寶石 (Al_2O_3) 基板上的 Bi_2Se_3 薄膜，其中包含了一步驟爐管磊晶和兩步驟爐管磊晶的薄膜。我們的實驗結果證明，採用兩步驟溫度設定沉積的 Bi_2Se_3 薄膜表現出顯著較高的質量。我們對硒化鉍薄膜進行了全面的分析，包括掃描電子顯微鏡 (SEM)、X 射線衍射 (XRD) 和 X 射線光電子能譜 (XPS)。兩步驟溫度磊晶方法在薄膜特性方面取得了優化的結果。經過量測，薄膜厚度通常具有約 0.7 微米。材料分析揭示了硒化鉍薄膜的化學鍵合和晶體結構與硒化鉍單晶體相似。

隨後，我們利用物理特性測量系統 (PPMS) 對材料薄膜進行磁輸運實驗，探討了拓撲絕緣體的弱反局域效應等特性。通過比較這些薄膜的磁輸運行為，我們對它們對外部磁場的響應和輸運特性有了更深入的了解。我們分析了一步驟磊晶和兩步驟磊晶的薄膜，觀察到兩步驟磊晶的薄膜表現出更明顯的拓撲絕緣體特徵，表現出更顯著的 WAL 效應、更高的 MR 值和對外部磁場更大的敏感性。此外，我們觀察到不同的場景，從理想情況 (表面貢獻占主導地位) 到更現實的情況 (大量貢獻占主導地位)。

通過將我們的研究結果與文獻中的數據進行比較，我們能夠揭示 Bi_2Se_3 的內在特性，並進一步證實兩步磊晶生長方法相比於一步磊晶過程可以得到質量更高的薄膜。

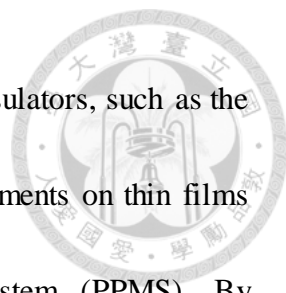
關鍵詞：硒化鉍，一步驟，兩步驟，表面質量分析，磁輸運，弱反局域化效應。

ABSTRACT



In recent years, there has been significant interest in topological insulators (TIs) in the fields of condensed matter physics and materials science, driven by their predicted unique physical properties and potential applications in spintronics and quantum computation. TIs are a class of materials characterized by an insulating bulk bandgap and conducting topological surface states (TSS) protected by time-reversal symmetry. In this study, we selected bismuth selenide (Bi_2Se_3), a three-dimensional topological insulator, as our target material. We compared Bi_2Se_3 films deposited on sapphire (Al_2O_3) substrates using one-step furnace heating and two-step furnace heating methods. Our experimental results convincingly demonstrate that Bi_2Se_3 films deposited with the two-step temperature setting exhibit significantly higher quality.

We conducted a comprehensive analysis of the Bi_2Se_3 films, including scanning electron microscopy (SEM), X-ray diffraction (XRD), and X-ray photoelectron spectroscopy (XPS). The two-step temperature deposition process yielded optimized results in terms of film characteristics. Typically, the thin films had a thickness of approximately 0.7 micrometers. Material analysis revealed a strong correlation between the chemical bonding and crystal structure of the Bi_2Se_3 thin films, resembling those of a single crystal of Bi_2Se_3 .



Subsequently, we explored the characteristics of topological insulators, such as the weak antilocalization effect, by conducting magnetotransport experiments on thin films of the material using the Physical Properties Measurement System (PPMS). By comparing the magnetotransport behaviors of these films, we gained a deeper understanding of their response to external magnetic fields and transport properties. We analyzed both one-step and two-step epitaxially grown films and observed that the two-step epitaxial growth demonstrated more pronounced characteristics of a topological insulator, showing a more significant WAL effect, higher MR values, and greater sensitivity to external magnetic fields. Additionally, we observed different scenarios, ranging from the ideal case (with dominant surface contributions) to more realistic situations (where bulk contributions prevail).

By comparing our findings with data reported in the literature, we were able to reveal the intrinsic properties of Bi_2Se_3 and further confirm that the two-step epitaxial growth method results in higher-quality and thin films with better topological characteristics compared to the one-step process.

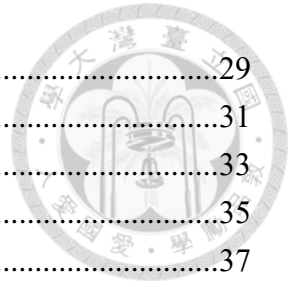
Key word: Bi_2Se_3 , one-step, two-step, surface quality analysis, magnetotransport, weak antilocalization effect.

CONTENTS



口試委員審定書	i
致謝	ii
摘要	iii
ABSTRACT	iv
CONTENTS	vi
LIST OF FIGURES	viii
Chapter 1. Introduction	1
1.1 Background and Overview	1
1.2 Motivation and Purpose	4
1.3 Thesis Outline	6
Chapter 2. Theory and Literature Review	8
2.1 Topological Insulators	8
2.2 Material Properties	10
2.2.1 Physical Properties of Bi ₂ Se ₃	10
2.2.2 Physical Properties of Al ₂ O ₃	12
2.3 Literature Review for Deposition Methods for Topological Material Thin Films	14
2.4 Literature Review for Magnetotransport of Topological Material	18
Chapter 3. Fabrication and Measurement	21
3.1 Bi ₂ Se ₃ Thin Film Deposition	21
3.2 Measurement Process Flow	25
3.3 Methods of Material Analysis	27
3.3.1 X-ray Diffraction	27

3.3.2	X-ray Photoelectron Spectroscopy	29
3.3.3	Scanning Electron Microscope.....	31
3.3.4	Photolithography	33
3.3.5	Electron Beam Evaporation.....	35
3.3.6	Physical Property Measurement System	37
Chapter 4.	Results and Discussion	39
4.1	Topological Thin Film Analysis	39
4.1.1	Scanning Electron Microscope Analysis	39
4.1.2	X-ray Photoelectron Spectroscopy Analysis	44
4.1.3	X-ray Diffraction Analysis	48
4.2	Magnetotransport of Topological Material.....	51
Chapter 5.	Conclusion	61
Reference	63



LIST OF FIGURES



Fig. 2.1 (a) Schematic representation of topological insulator material: bulk is insulating where surface is conducting or metallic behavior. (b) Energy dispersion of the spin non-degenerate surface state of a 3D TI forming a 2D Dirac cone. Energy band diagram of: (c) insulator with large band gap and (d) metallic or conducting with no gap between conduction band and valence band. (e) Dispersion of a topological insulator, showing Dirac dispersing surface states lying in the bulk band gap.9

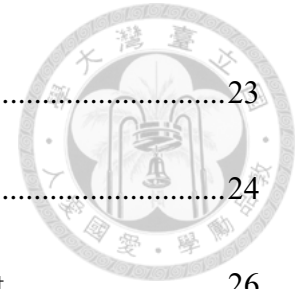
Fig. 2.2 (a) Hexagonal crystal structure of Bi_2Se_3 where a quintuple layer with $\text{Se}^1\text{-Bi-}\text{Se}^2\text{-Bi-}\text{Se}^1$ sequence is presented by the blue square. (b) Top view along the z-direction. One quintuple layer's triangle lattice has three distinct positions, denoted A, B, and C. (c) Side view of the quintuple layer structure. The stacking order of Bi and Se atomic layers along the z-direction. 11

Fig. 2.3 Crystal structure of the single-crystal sapphire.[15] 13

Fig. 3.1 Schematic drawing of a horizontal tube furnace.22

Fig. 3.2 Temperature variation diagram of the furnace, (a) one-step growth (b) two-step growth.....23

Fig. 3.3 Temperature color distribution and path of deposited target material in the furnace.



.....23

Fig. 3.4 SEM of Bi_2Se_3 epitaxial thin film thickness side-view.....24

Fig. 3.5 Process flow for sample preparation for PPMS measurement.26

Fig. 3.6 Composition of an XRD Diffractometer.[34].....27

Fig. 3.7 Schematic representation of the Bragg equation.[34]28

Fig. 3.8 Schematic of an XPS instrument.[35]29

Fig. 3.9 Principle of XPS.....30

Fig. 3.10 Electron beam-sample interaction and emitted signal.[36].....31

Fig. 3.11 Schematic of Electron Beam Evaporation System.[38]35

Fig. 3.12 Function of the PPMS - Quantum Design PPMS-16T.[39]38

Fig. 4.1 The growth of Bi_2Se_3 on a Al_2O_3 substrate under different conditions, with target weights of 300mg (a)-(d) and 600mg (e)-(h), and deposition times of 1 hour, 1 hour 30 minutes, 2 hours 30 minutes, and 4 hours, respectively.....40

Fig. 4.2 Photograph of (a)one-step (b) two-step Bi_2Se_3 thin film surface.41

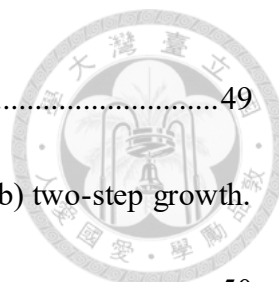
Fig. 4.3 SEM of (a)one-step (b) two-step Bi_2Se_3 thin film surface.....42

Fig. 4.4 XPS patterns of Bi_2Se_3 thin films deposited on Al_2O_3 substrates.45

Fig. 4.5 XPS spectra of one-step Bi_2Se_3 thin film: (a) Se 3d peaks; (b) Bi 4f peaks.46

Fig. 4.6 XPS spectra of two-step Bi_2Se_3 thin film: (a) Se 3d peaks; (b) Bi 4f peaks.46

Fig. 4.7 XRD patterns of Bi_2Se_3 films deposited on Al_2O_3 substrates, (a) one-step growth,



(b) two-step temperature growth.49

Fig. 4.8 XRD patterns of Bi_2Se_3 (0006) peak, (a) one-step growth, (b) two-step growth.
.....50

Fig. 4.9 Resistance vs temperature curves taken from 5 to 300 K: (a) one-step growth, (b)
two-step growth.52

Fig. 4.10 Perpendicular MR for the film at 5 K: (a) one-step growth, (b) two-step growth.
Parallel MR for the film at 5 K: (c) one-step growth, (d) two-step growth.53

Fig. 4.11 MR of thin film at different temperatures: (a) one-step growth, (b) two-step
growth.....56

Fig. 4.12 Magnetoconductance analysis of Bi_2Se_3 single crystal measured at different
temperatures: (a) one-step growth, (b) two-step growth. The black solid line
represents the HLN fitting.58

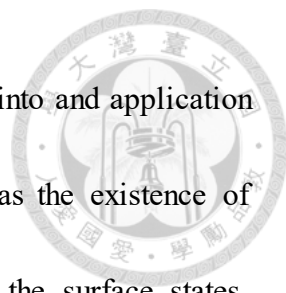
Chapter 1. Introduction



1.1 Background and Overview

In condensed matter physics, topological materials have emerged as a fascinating and swiftly developing field of study. These materials exhibit unique electronic properties that are fundamentally different from conventional insulators, semiconductors, and metals. Topological materials are distinguished by the presence of topological invariants, which protect robust surface or edge states that are highly conductive and immune to backscattering. One of the most well-known and extensively studied classes of topological materials is topological insulators (TIs). TIs are materials that possess an insulating bulk band gap but host conducting surface states. These surface states exhibit a linear dispersion relationship, similar to relativistic Dirac fermions, and are protected by time-reversal symmetry. Due to their unique electronic structure, topological insulators have potential applications in various fields, including spintronics, quantum computing, and energy conversion.

Bismuth selenide (Bi_2Se_3) is one of the pioneering and extensively studied topological insulator materials. At the surface or interface of Bi_2Se_3 , a highly conductive two-dimensional (2D) electron gas forms due to the presence of topological surface states. These surface states are protected by time-reversal symmetry and exhibit a linear



dispersion near the Fermi level. Bi_2Se_3 is a good option for research into and application of topological phenomena due to its special characteristics, such as the existence of topological surface states. In order to preserve and fully exploit the surface states, researchers have investigated different approaches to fabricate topological material thin films, including methods such as mechanical exfoliation, molecular beam epitaxy (MBE), metal-organic chemical vapor deposition (MOCVD), physical vapor deposition (PVD), chemical vapor deposition (CVD), pulsed laser deposition (PLD).

Having achieved high-quality topological thin films, researchers have shifted their focus to studying the behaviors of these materials. Transport studies of TIs have provided valuable insights into the unique quantum phenomena exhibited by their topological surface states. These phenomena have been observed in various TIs, leading to intriguing experimental results. For instance, Aharonov-Bohm oscillations have been observed in Bi_2Se_3 nanoribbons[1]. Additionally, weak anti-localization (WAL) has been identified in Bi_2Se_3 and Bi_2Te_3 thin films, indicating the presence of coherent electron backscattering due to spin-momentum locking in the surface states[2-4], and 2D Shubnikov-de Haas (SdH) oscillations have also been recorded[5, 6].

In this thesis, we concentrate on the two-step epitaxial growth method for depositing Bi_2Se_3 thin films on sapphire (Al_2O_3) substrates, aiming to achieve enhanced film quality. Subsequently, we explore their magnetotransport properties using a Physical Property


Measurement System (PPMS) to investigate the behavior of topological insulators.



1.2 Motivation and Purpose



A topological insulator material with unique electronic properties makes it desirable for various technological applications. However, achieving high-quality Bi_2Se_3 films with controlled thickness and morphology is crucial for realizing their full potential in practical devices. The use of Al_2O_3 as a substrate in thin film deposition is motivated by its excellent thermal and mechanical properties, as well as its widespread availability. Al_2O_3 offers a stable and robust platform for growing Bi_2Se_3 films, providing an opportunity to study their growth mechanisms and optimize the deposition process. Among the various deposition methods, the two-step deposition method is particularly intriguing due to its potential to improve film quality and control the growth process. Exploring the two-step method for depositing Bi_2Se_3 on Al_2O_3 holds promise for obtaining high-quality films with enhanced structural and electronic properties. The purpose of this research is multifold. Firstly, it aims to investigate the growth process of Bi_2Se_3 thin films on Al_2O_3 using the two-step method. By systematically varying deposition parameters and analyzing the resulting film characteristics, the study aims to understand the underlying mechanisms involved in film nucleation, growth, and structural evolution. Furthermore, the research seeks to characterize the structural, morphological, and electrical properties of the deposited Bi_2Se_3 films. By employing techniques such as scanning electron



microscopy (SEM), X-ray diffraction (XRD), X-ray photoelectron spectroscopy (XPS), and physical property measurement system (PPMS), the study aims to assess the film quality, crystal structure, surface morphology, conductivity, and topological characteristics. These characterizations provide valuable insights into the film's performance and its potential for device applications. Ultimately, the findings of this research contribute to a broader understanding of the growth and properties of Bi_2Se_3 films on Al_2O_3 . The optimized deposition conditions obtained from this study can lead to high-quality thin film materials with excellent topological characteristics, which can be applied in various future applications.

1.3 Thesis Outline



This section's primary purpose is to elucidate the thesis's organization.

In Chapter 1, we provide an introduction to the research by giving background information and an overview of the study. The motivation and purpose behind investigating topological insulators (TIs) are also explained.

Chapter 2 is dedicated to the theoretical framework and literature review. We delve into the concept of topological insulators and explore their unique material properties. The chapter also includes a comprehensive literature review on various deposition methods used to create thin films of topological materials. Additionally, we review the existing literature on magnetotransport phenomena observed in topological materials.

Chapter 3 focuses on the fabrication process and measurement setup. The detailed procedure for depositing Bi_2Se_3 thin films is outlined. Furthermore, we describe the preparation process for magnetotransport measurements using the Physical Properties Measurement System (PPMS). Various instruments and analysis techniques used throughout the study are also discussed.

Chapter 4 presents the results obtained and initiates in-depth discussions. We analyze the properties of the topological thin film, including the growth process of Bi_2Se_3 films, X-ray Photoelectron Spectroscopy (XPS) analysis, and X-ray Diffraction (XRD) analysis.

Subsequently, we investigate the magnetotransport behavior of topological materials.

Lastly, in Chapter 5, we draw conclusions based on our findings and discuss the future prospects for this research. The implications of our results are discussed, and potential directions for further investigations in the field of topological insulators are outlined.

Chapter 2. Theory and Literature

Review



2.1 Topological Insulators

Topological insulators (TIs), unlike conventional insulators, have conducting surface or edge states within the bulk band gap between the valence and conduction bands, as shown in Figure 2.1. These surface states are protected by time-reversal symmetry and resistant to disorder, which makes them highly desirable for applications in spintronics, quantum computation, and energy conversion.

The mathematical concept of topology plays a central role in comprehending and describing topological insulators. In the context of condensed matter physics, topology refers to the global properties of the electronic structure of a material that remain unchanged under continuous deformations. This topological protection guarantees the stability of the surface or edge states and renders them immune to backscattering, even in the presence of impurities and imperfections.

Typically, the electronic structure of topological insulators is distinguished by a bulk band gap and gapless surface or edge states. These surface states possess distinctive characteristics, such as a linear dispersion relationship and spin-momentum locking, in



which the electron's spin is bound perpendicular to its momentum. The spin-momentum locking results from the strong spin-orbit coupling in topological insulators and gives rise to fascinating phenomena like the quantum spin Hall effect.

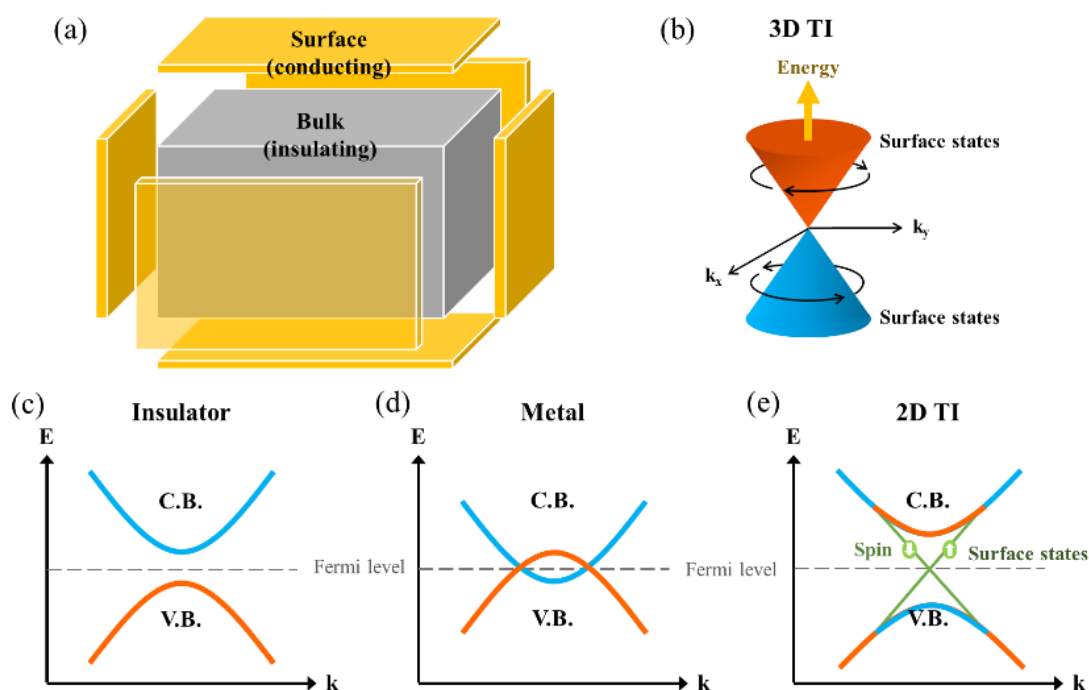


Fig. 2.1 (a) Schematic representation of topological insulator material: bulk is insulating where surface is conducting or metallic behavior. (b) Energy dispersion of the spin non-degenerate surface state of a 3D TI forming a 2D Dirac cone. Energy band diagram of: (c) insulator with large band gap and (d) metallic or conducting with no gap between conduction band and valence band. (e) Dispersion of a topological insulator, showing Dirac dispersing surface states lying in the bulk band gap.



2.2 Material Properties

2.2.1 Physical Properties of Bi_2Se_3

Bismuth selenide (Bi_2Se_3), a compound belonging to the family of three-dimensional TIs, has emerged as one of the most promising materials in this class. Bi_2Se_3 possesses several appealing characteristics that make it highly suitable for various applications. It features a rhombohedral crystal structure with the space group D_{3d}^5 ($R\bar{3}m$) with five atoms in one unit cell. The atomic structure of Bi_2Se_3 consists of weakly covalent quintuple layers, which consist of five atoms: two equivalent Se atoms (represented by Se^1), two equivalent Bi atoms, and a third Se atom (represented by Se^2), as depicted in Figure 2.2. The coupling between two atomic layers within one quintuple layer is robust, whereas the coupling between two quintuple layers is significantly weaker and predominately of the van der Waals type [7]. With a relatively wide bandgap of 0.35 eV, Bi_2Se_3 enables efficient control of the transport properties through tuning the Fermi level position within the bandgap.[8, 9] Additionally, Bi_2Se_3 displays distinct Dirac cones in the TSS, offering a platform for investigating novel quantum phenomena as the quantum spin Hall effect and topological superconductivity. Another advantage of Bi_2Se_3 is its remarkable thermoelectric performance at temperatures near room temperature[10, 11], making it promising for energy conversion and waste heat recovery applications.

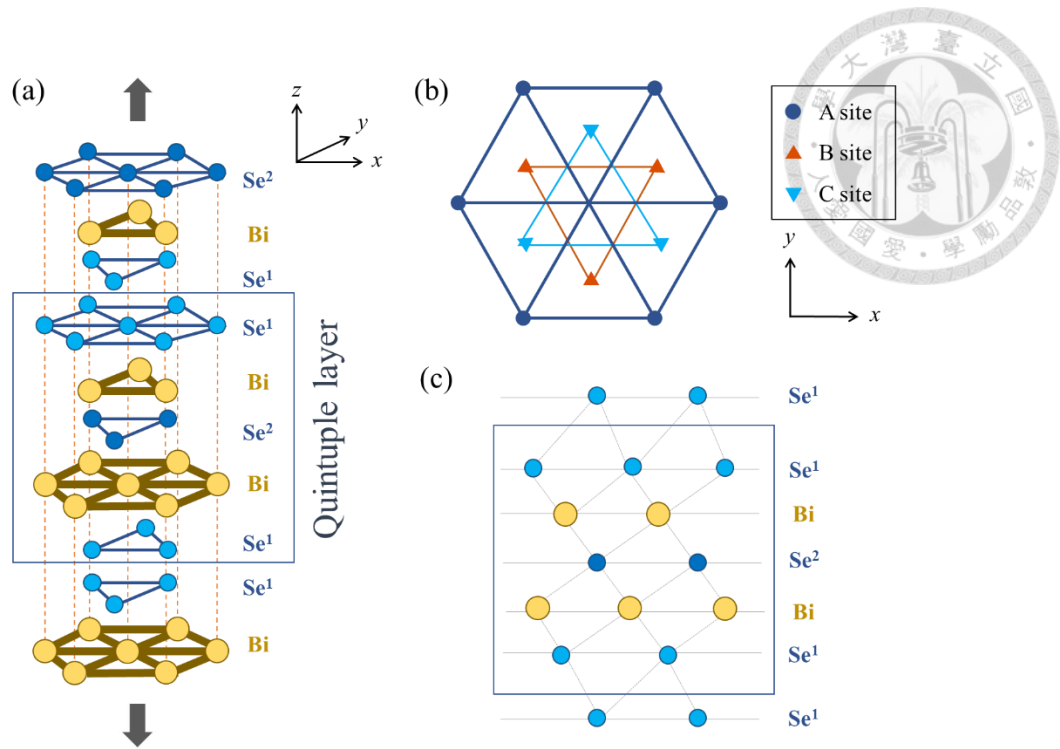


Fig. 2.2 (a) Hexagonal crystal structure of Bi_2Se_3 where a quintuple layer with Se^1 -Bi- Se^2 -Bi- Se^1 sequence is presented by the blue square. (b) Top view along the z -direction. One quintuple layer's triangle lattice has three distinct positions, denoted A, B, and C. (c) Side view of the quintuple layer structure. The stacking order of Bi and Se atomic layers along the z -direction.



2.2.2 Physical Properties of Al₂O₃

In order to fully unleash the potential of Bi₂Se₃ in practical devices, optimizing the growth of high-quality films on suitable substrates is crucial. Among the wide range of substrate options, c-plane sapphire (Al₂O₃) is the most commonly used substrate for growing Bi₂Se₃ films. Although there is a considerable lattice mismatch (~15%) between c-plane Al₂O₃ and Bi₂Se₃, leading to potential structural defects like twin defects, antiphase domains, or mosaicity-twists[12], it still possesses the same in-plane lattice structure as Bi₂Se₃. Despite this mismatch, Al₂O₃ offers several advantages that make it an attractive choice for Bi₂Se₃ growth. Al₂O₃ is a transparent material with excellent mechanical toughness, strength, and outstanding thermal and dielectric properties. Its corrosion resistance and stability even at high temperatures, with a melting point of up to 2030°C, make it highly desirable for various applications. The well-established and cost-effective growth process of Al₂O₃ crystals along the C-axis results in a smooth and flawless surface, ensuring a high-quality film-substrate interface during the deposition of thin films. Additionally, the exceptional insulation properties of Al₂O₃ prevent any interference from the substrate, enabling reliable electrical transport measurements of Bi₂Se₃ thin films and making them suitable for room temperature applications[13, 14]. Given these benefits, c-plane Al₂O₃ remains a favorable choice for epitaxial growth of

Bi₂Se₃ films despite the lattice mismatch.

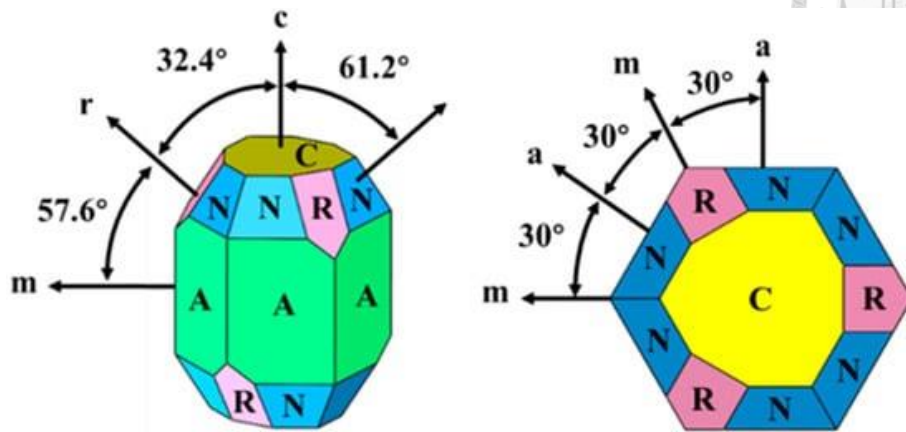


Fig. 2.3 Crystal structure of the single-crystal sapphire.[15]

2.3 Literature Review for Deposition Methods for



Topological Material Thin Films

Incorporating TI thin films into electronic devices necessitates high mobility of non-trivial surface carriers and a low bulk carrier density. However, defects on the surface can reduce the mobility of surface states, limiting their contribution to transport. Therefore, developing high-quality thin films is crucial to fully harness the potential of TIs in technological applications. Researchers have explored various approaches to fabricate crystalline thin films, including methods like mechanical exfoliation, molecular beam epitaxy (MBE), metal-organic chemical vapor deposition (MOCVD), physical vapor deposition (PVD), chemical vapor deposition (CVD), and pulsed laser deposition (PLD) [11, 16-20], among others.

Molecular beam epitaxy (MBE) stands out among the deposition techniques as a popular technique for producing high-quality topological thin films. By layer-by-layer depositing atoms or molecules, MBE enables fine control over the film's development while assuring good crystallinity and stoichiometry. In numerous researches, topological thin films with variable carrier concentrations and thicknesses were successfully grown using MBE.

Another popular technique is pulsed laser deposition (PLD), which employs a high-

energy laser to ablate a target material and deposit it onto the substrate. The production of topological thin films with distinct crystal structures and sharp interfaces has been successfully shown via PLD.

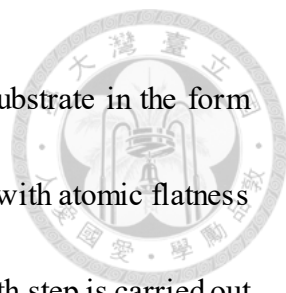


Topological thin films have also been created using physical vapor deposition (PVD) techniques such as thermal evaporation and electron beam evaporation. These techniques offer simplicity and versatility, making them suitable for both laboratory-scale research and industrial applications.

Another deposition technique that is frequently used in the development of topological thin films is sputtering. Particularly magnetron sputtering makes it possible to manage the film thickness and deposit films with remarkable uniformity.

Chemical vapor deposition (CVD) is emerging as a promising technique for large-scale production of topological thin films due to its scalability and cost-effectiveness. High-quality films can be deposited via CVD by chemical interactions between precursor gases and the surface of the substrate[21].

Another two-step growth method[22, 23] is employed to improve the film quality and control imperfections in topological thin films, aiming to produce high-quality topological material thin films. The main steps of this method involve a low-temperature growth followed by a high-temperature growth. Firstly, the low-temperature growth step aims to form an atomically flat surface on the substrate. This step is typically performed



using MBE technique, where Bi and Te atoms are deposited on the substrate in the form of a low-energy beam. The intention of this step is to create a surface with atomic flatness and reduce the formation of defects. Next, the high-temperature growth step is carried out to further increase the thickness of the Bi_2Te_3 thin film. In this step, Bi and Te atoms are deposited with higher energy onto the previously formed atomically smooth surface. This promotes higher crystalline quality and the formation of larger domain structures in the thin film. Researchers have observed that Bi_2Te_3 films grown using this method exhibit large-area micrometer-scale domain structures and wide concentric atomic flat terraces on the surface. Moreover, this method significantly reduces the three-dimensional structure density in the thin film, improving the crystalline quality and reducing dislocations or island merging. The optimal temperature for the low-temperature growth step is 195°C , while the optimal temperature for the high-temperature growth step is 240°C .

The literature analysis concludes by highlighting the variety of deposition techniques available for topological material thin films, each with specific benefits and drawbacks. The development of topological materials research and possible technology applications has been facilitated by researchers' ongoing efforts to optimize these fabrication processes for topological thin films with improved electrical and transport properties.

In this study, we employed the advantages of a two-step temperature approach to

deposit Bi_2Se_3 on Al_2O_3 substrates. The deposition was carried out using a conventional tube-furnace CVD system. Compared to other methods, CVD is a cost-effective option.



2.4 Literature Review for Magnetotransport of

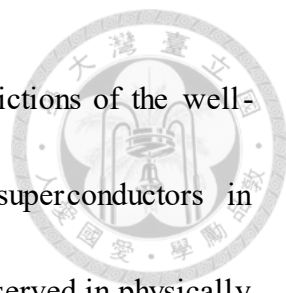


Topological Material

The study of magnetotransport in topological materials has shed light on fascinating phenomena associated with their linearly dispersing semi-metallic surface states. Among these phenomena, the presence of weak anti-localization (WAL) in the magnetoresistance of three-dimension TIs at low magnetic fields has emerged as a crucial area of investigation. WAL refers to the quantum interference effect that leads to a reduction in the scattering of charge carriers in certain materials, resulting in non-saturating magnetoresistance behavior.

At high magnetic fields, researchers have extensively studied linear magnetoresistance (LMR) in topological insulators, particularly in materials like Bi_2Te_3 , Bi_2Se_3 , and other TIs[24-28]. The non-saturating LMR at high magnetic fields has been a subject of interest due to its potential applications in magnetic field sensors. Additionally, logarithmic magnetoresistance arising from WAL has been observed at low magnetic fields and low temperatures in various topological insulators[2, 3, 29-31]. This logarithmic behavior tends to diminish at higher temperatures, reflecting the influence of temperature on the transport properties of these materials.

The coexistence of LMR with quantum oscillations in certain topological



insulators has intrigued researchers, as it deviates from the predictions of the well-known Abrikosov's theory, which addresses the behavior of superconductors in magnetic fields. To explain the non-oscillatory LMR behavior observed in physically inhomogeneous samples, an alternative classical theory proposed by Little and Parishwood has been employed. This theory has proven to be effective in describing the transport characteristics of narrow or zero bandgap systems like TIs.

To understand the weak anti-localization phenomenon in the linearly dispersing surface states of TIs, researchers have utilized the Hikami-Larkin-Nagaoka (HLN) model[32]. This model accounts for the quantum interference effects that contribute to the observed WAL behavior and provides important information about the quantum interference effects and electronic properties of the material. By applying the HLN model to the magnetotransport data, researchers can extract valuable insights into the scattering mechanisms and the characteristics of charge carriers in the topological insulator.

The literature review reveals a wealth of fascinating magnetotransport phenomena in topological materials. The interplay between LMR, quantum oscillations, and WAL in topological materials has become an exciting area of research. These findings provide valuable insights into the unique transport properties of topological insulator surface states, highlighting their potential for various applications in spintronics and

quantum computing. Further investigation into these transport phenomena promises to deepen our understanding of the electronic behavior of topological insulators and may lead to novel technological advancements.



Chapter 3. Fabrication and Measurement



3.1 Bi₂Se₃ Thin Film Deposition

In a tube furnace setup, Bi₂Se₃ films were deposited on single-crystalline substrates. As seen in Figure 3.1, a horizontal tube furnace is equipped with a three-zone heater and an Ar gas mass flow controller. Before being used for the deposition of thin films, Al₂O₃ substrates were cleaned using a normal technique. This was done so that single crystalline Bi₂Se₃ thin films could be grown on Al₂O₃ (0001) substrates. The Al₂O₃ substrate was sequentially immersed in acetone and methanol at 100°C for five minutes each, followed by rinsing with isopropanol and drying using an N₂ stream. This was done so that any possible dirt and grime could be removed from the surface. Weighing and depositing in the middle of the quartz tube furnace 600 mg of powder that contains 99.999% Bi₂Se₃. Both of the sides of the furnace, which is 30 centimeters away from the center, were stocked with Al₂O₃ substrates. Approximately 5×10^{-2} torr was the initial pressure identified inside the tube. The gas flow controller was opened to allow an Ar gas flow rate of 150 sccm, causing the tube pressure to increase by 250 torr. Subsequently, the pump switch was turned on again to begin the pumping process. This procedure

effectively cleaned the tube. Following the tube cleaning, the pressure inside the tube was reduced to less than 5×10^{-3} torr through further pumping[33].

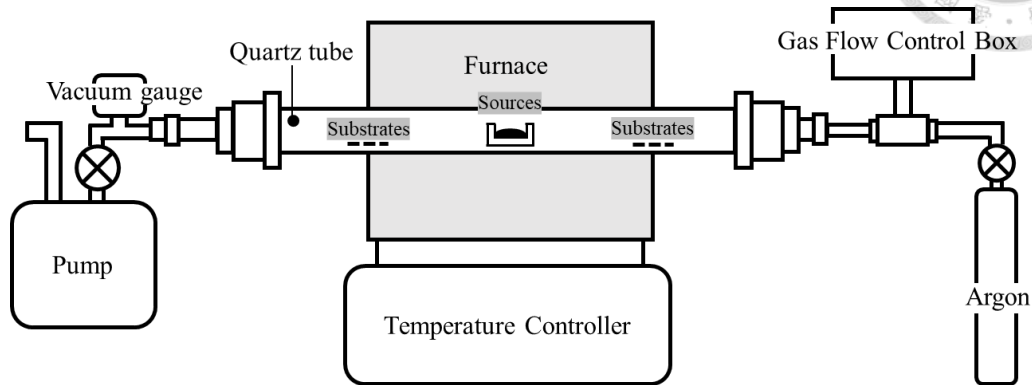


Fig. 3.1 Schematic drawing of a horizontal tube furnace.

Figure 3.2 (a) illustrates the temperature variation diagram of the three regions of the furnace tube during the one-step growth process. Using 600 mg target, the center of the furnace was heated to 800 °C and the substrates at both sides has a temperature around 700 °C. The Bi_2Se_3 growth time is around 150 mins. In order to obtain a smooth surface so that surface defects may be suppressed, a second step was introduced to desorb and volatilize the surface impurities incurred during the growth. The temperature in the center of the furnace was decreased to 300 °C, while that at the substrates of both sides is 650 °C, as shown in Figure 3.2 (b).

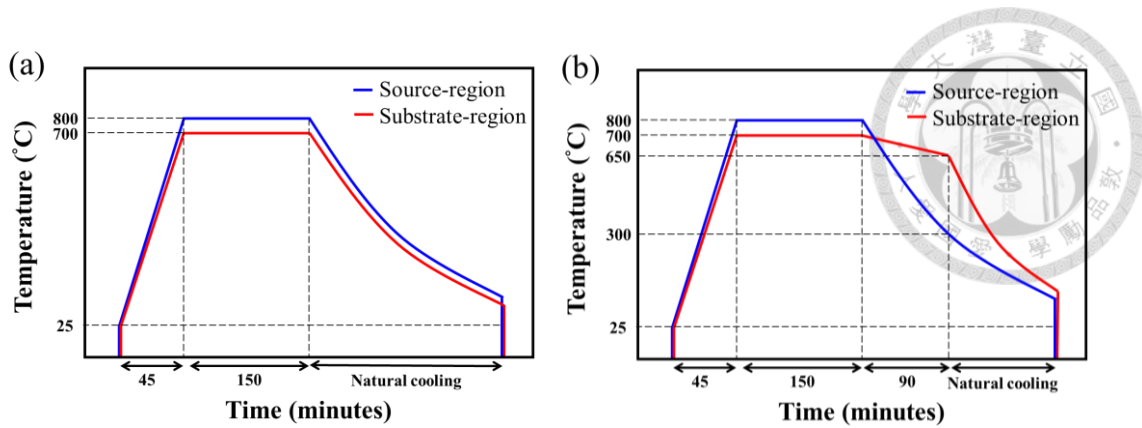


Fig. 3.2 Temperature variation diagram of the furnace, (a) one-step growth (b) two-step growth.

Figure 3.3 illustrates the temperature color distribution trend inside the furnace and the path of the target material deposited on the substrate after heating. Then obtain a single crystal thin film of Bi_2Se_3 measuring between 500 to 700 nm thickness, as observed in Figure 3.4. Moreover, to prevent the deposition of airborne impurities onto the substrates, the temperature of the second step was adjusted accordingly. By lowering the temperature in the central area to 20°C , the likelihood of such a scenario occurring could be largely mitigated.

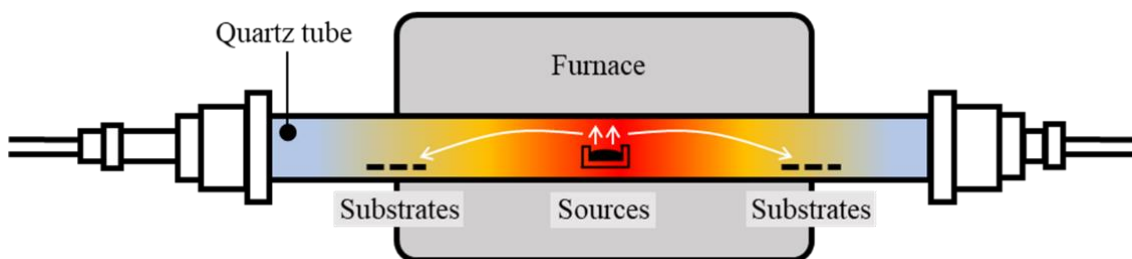


Fig. 3.3 Temperature color distribution and path of deposited target material in the furnace.

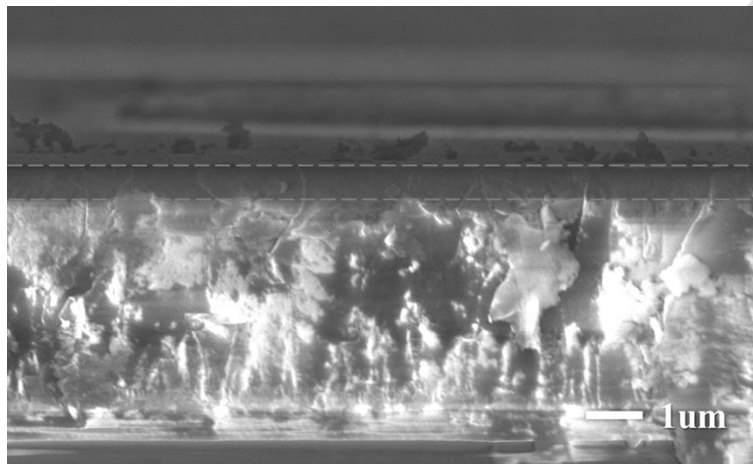
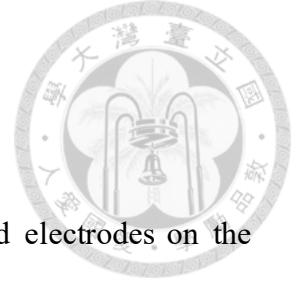


Fig. 3.4 SEM of Bi₂Se₃ epitaxial thin film thickness side-view.

3.2 Measurement Process Flow



In order to investigate magnetic transport, we have deposited electrodes on the already epitaxially grown and surface-smoothed thin film samples. This enables subsequent wire bonding and measurements in the physical property measurement system (PPMS) system. The process flow, as shown in Figure 3.5, begins with the conventional cleaning of the substrate to remove impurities from the Al_2O_3 substrate. Following this, the Bi_2Se_3 thin film is epitaxially grown on the substrate using the process parameters described in Section 3.1. Once we have obtained the desired thin film, we can proceed with further fabrication. The prepared Bi_2Se_3 thin film serves as the foundation for depositing electrodes. A metal stack of Ti/ Au with thicknesses of 10/200 nm, respectively, is deposited onto the film. After depositing the electrodes on the sample, we perform wire bonding to attach the sample to the corresponding electrodes on the PCB board. The wire bonding is done to ensure proper electrical connections. Once the sample is prepared, we can proceed with the measurements using the PPMS system.

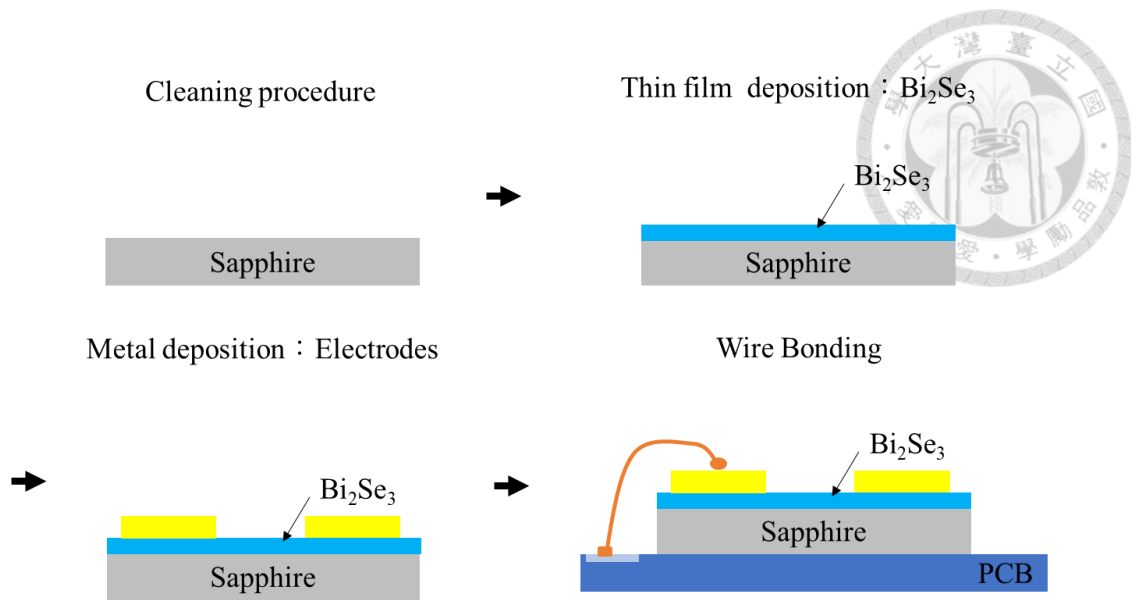


Fig. 3.5 Process flow for sample preparation for PPMS measurement.



3.3 Methods of Material Analysis

3.3.1 X-ray Diffraction

X-ray diffraction (XRD) is a widely used technique for the structural characterization of materials. The composition of an XRD diffractometer is shown in Figure 3.8, which includes the essential components used in the analysis process. It provides valuable insights into the arrangement of atoms in a crystal lattice, allowing researchers to determine the crystal structure, phase composition, and crystalline quality of a sample. XRD is based on the principles of Bragg's law and the interference of X-rays scattered by the crystal lattice.

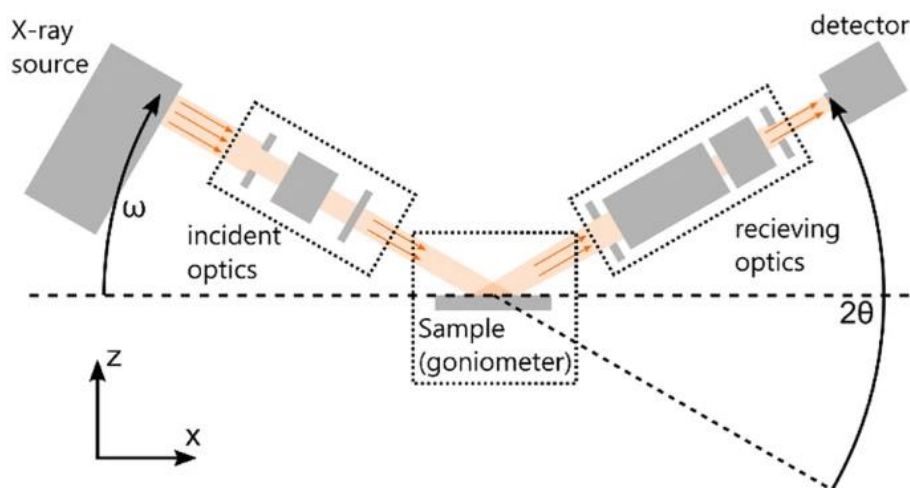


Fig. 3.6 Composition of an XRD Diffractometer.[34]

In our study, we are using Cu K α radiation with a wavelength of 1.5418 Å. According to Bragg's law ($n\lambda = 2d \sin\theta$), constructive interference occurs when the path difference



between X-rays scattered from successive crystal planes is an integer multiple of the wavelength. This allows us to calculate the interplanar spacing (d) based on the diffraction angle (θ), as shown in Figure 3.7.

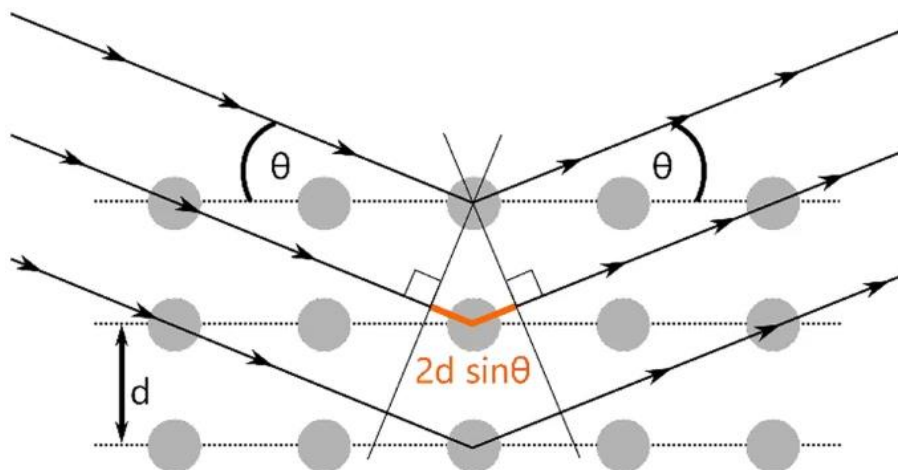


Fig. 3.7 Schematic representation of the Bragg equation.[34]

The resulting XRD pattern provides information about the crystal structure, including the lattice parameters, symmetry, and orientation of the crystal. It also allows for the identification of different crystal phases present in a sample. Additionally, the intensity and width of the diffraction peaks provide insights into the crystalline quality, strain, and defects within the material. XRD is also a non-destructive technique, making it highly suitable for helping us understand the characteristics and behavior of materials.



3.3.2 X-ray Photoelectron Spectroscopy

X-ray Photoelectron Spectroscopy (XPS), also known as Electron Spectroscopy for Chemical Analysis (ESCA), is a powerful surface analysis technique used to investigate the elemental composition and chemical states of materials. It provides valuable insights into the surface chemistry, bonding characteristics, and electronic properties of a wide range of solid materials, including metals, semiconductors, polymers, and organic compounds.

In our study, we utilize an XPS instrument, as shown in Figure 3.8. The XPS instrument consists of several essential components, including an X-ray source, a sample chamber, an energy analyzer, and a detector. The X-ray source, in our case, is an Al $K\alpha$ monochromator, which emits a monochromatic X-ray beam. This X-ray beam is directed onto the sample's surface in the sample chamber.

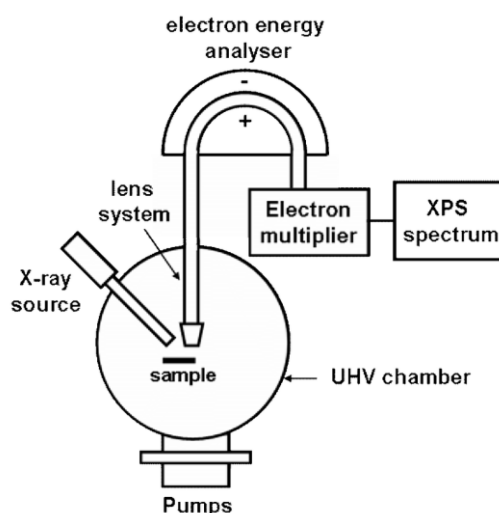
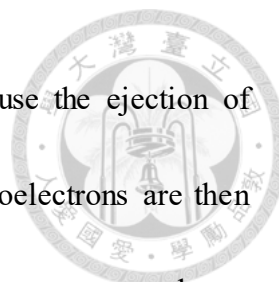


Fig. 3.8 Schematic of an XPS instrument.[35]



When the X-rays interact with the sample's surface, they cause the ejection of photoelectrons from the outermost atomic layers. The emitted photoelectrons are then accelerated towards the energy analyzer, which measures their kinetic energy, as shown in Figure 3.9. By analyzing the energy spectrum of the emitted photoelectrons, we can identify the elements present in the sample and determine their chemical states. XPS provides valuable information about the elemental composition, chemical environment, and bonding characteristics of the sample's surface. It can distinguish between different oxidation states, identify surface contaminants or adsorbates, and detect changes in chemical states induced by surface treatments or reactions.

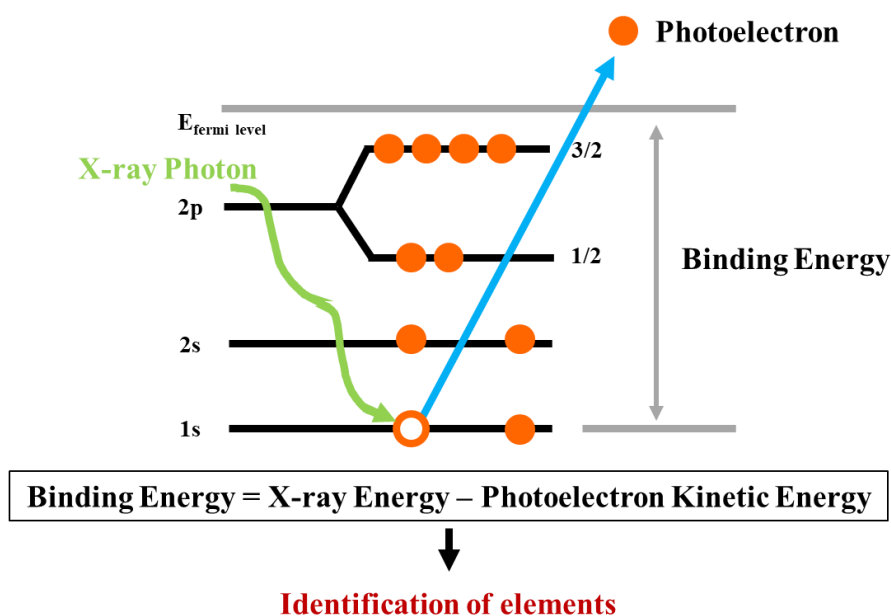
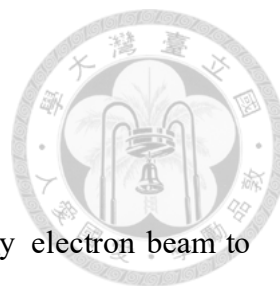


Fig. 3.9 Principle of XPS.



3.3.3 Scanning Electron Microscope

The scanning electron microscope (SEM) utilizes a high-energy electron beam to scan the sample, generating images. It consists of three main components: the vacuum system, electron beam system, and imaging system. When the electrons interact with the sample, they give rise to secondary electrons, backscattered electrons, and characteristic X-rays, as shown in Figure 3.10. These signals are collected by one or more detectors to create images, which are then displayed on a computer screen.

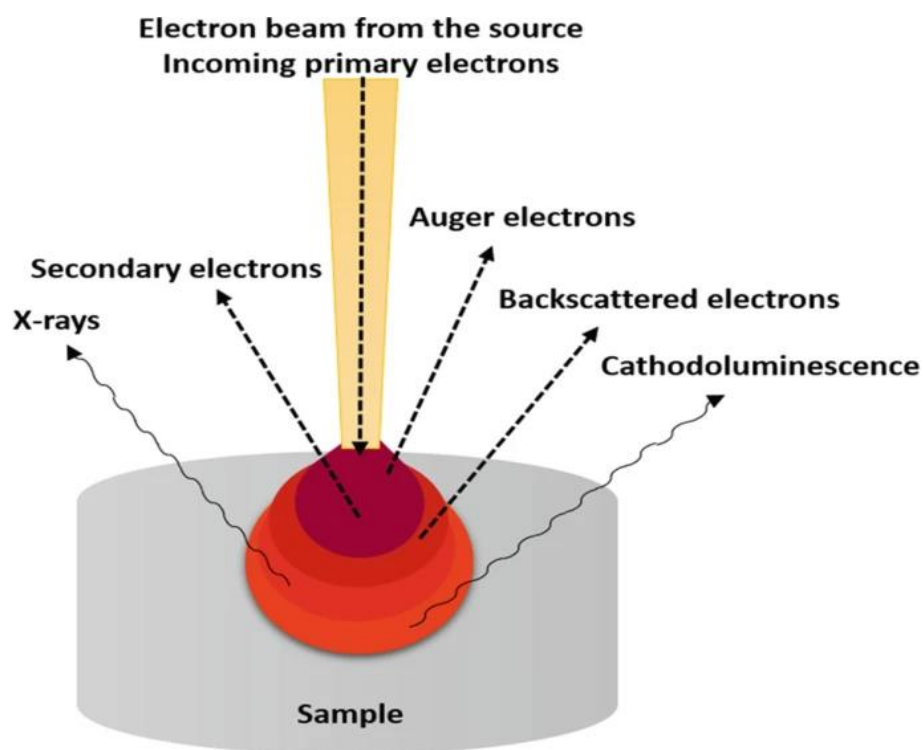
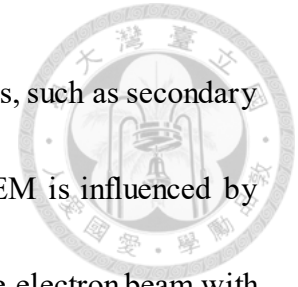


Fig. 3.10 Electron beam-sample interaction and emitted signal.[36]

Upon striking the sample's surface, the electron beam penetrates the material to a depth of a few microns, depending on the accelerating voltage and sample density. This

interaction inside the sample leads to the production of various signals, such as secondary electrons and X-rays. The maximum resolution achievable in an SEM is influenced by factors such as the electron spot size and the interaction volume of the electron beam with the sample. While atomic resolution is not possible with SEM, some instruments can achieve resolution below 1 nm. Generally, modern full-sized SEMs offer resolution in the range of 1-20 nm.





3.3.4 Photolithography

The photolithography process involves transferring designed patterns from a mask onto the sample. To complete the photolithography process, several steps are required, including spin-coating photoresist, aligning patterns on the mask with those on the sample, exposure, and finally developing the photoresist.

During spin-coating, the photoresist is dispensed onto the sample, which is positioned on the spin-coater. Initially, the rotation rate is low, and then it is increased to achieve a thin and uniform film. The thickness of the photoresist after spin-coating depends on factors such as viscosity, surface tension, spin rate, spin time, and acceleration rate. The square of the thickness of the photoresist is approximately inversely proportional to the spin rate.

Photoresist can be categorized into positive and negative tones. In positive-tone resist, the exposed area to UV light dissolves into the developer, while in negative-tone resist, the exposed area becomes insoluble. Photoresist usually consists of polymer, solvent, sensitizer, and additives. The polymer provides adhesion to the sample's surface, the solvent dissolves the polymer and sensitizer to reduce the resist's thickness, and the sensitizer regulates the photochemical reaction during UV light exposure.

For positive resist, the sensitizer undergoes dissociation and breaks the cross-links

after exposure to UV light, transforming it into an aqueous-base-soluble material that can be developed. In negative resist, the sensitizer contains organic material with an N3 group, and during exposure, the release of N₂ gas leads to cross-linking of the bonding, enhancing chemical resistance.[37]

In this research, the photolithography process uses various types of photoresists, including novolak-based s1813 (MICROPOSIT), polydimethylglutarimide (PMGI), and LOR (MicroChem). These photoresists are all positive-tone resists.



3.3.5 Electron Beam Evaporation

Electron Beam Evaporation is a widely used physical vapor deposition (PVD) technique for depositing thin films onto substrates. It involves the use of an electron beam to heat a solid material, causing it to vaporize and form a thin film on the substrate.

In the Electron Beam Evaporation process, a high-energy electron beam is generated and directed towards a target material, which is typically placed in a vacuum chamber. The electron beam bombards the target, causing its atoms or molecules to be ejected from the surface and form a vapor. This vapor then condenses onto the substrate, which is positioned in close proximity to the target, as shown in Figure 3.11.

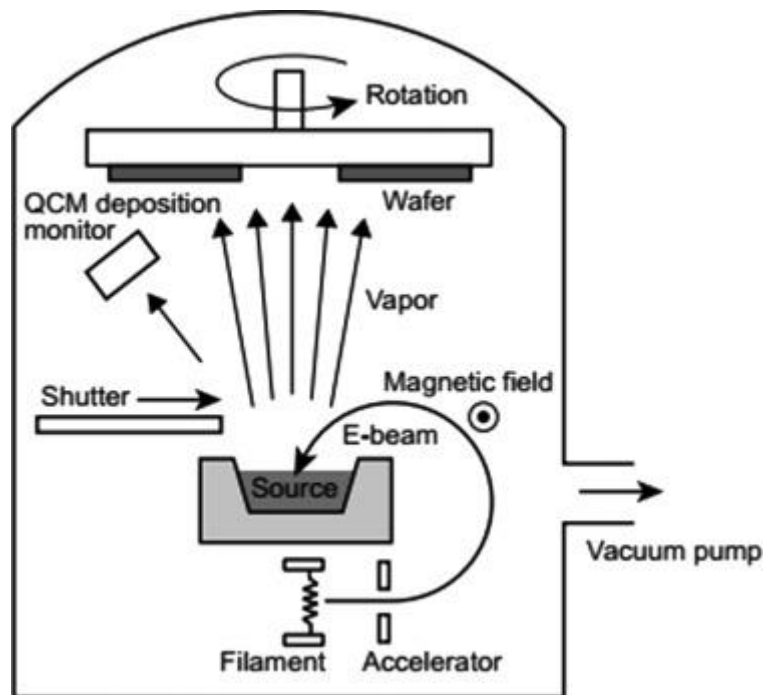
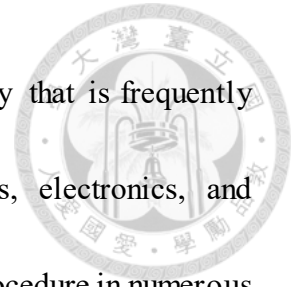


Fig. 3.11 Schematic of Electron Beam Evaporation System.[38]

High deposition rates, great film homogeneity, and superb composition control are

all benefits of electron beam evaporation. It is a flexible technology that is frequently utilized in many different industries, including coatings, optics, electronics, and semiconductor production. Electron beam evaporation is a crucial procedure in numerous scientific and industrial applications because it is particularly useful for producing high-quality films with exact control over thickness and composition.



3.3.6 Physical Property Measurement System



A flexible and sophisticated experimental platform that is frequently used in condensed matter physics, materials science, and other scientific fields is the Physical Property Measurement System (PPMS). The PPMS is a tool that Quantum Design developed to measure a wide range of physical properties of materials in various temperature, magnetic field, and pressure environments. Figure 3.12 shows that the Quantum Design PPMS-16T PPMS model we used has a superconducting magnet that can make magnetic fields up to 16 Tesla strong. This lets researchers study the magnetic properties of materials. It also provides accurate temperature control over a large range, from temperatures close to absolute zero to as high as 400 K, enabling the study of materials under various temperature regimes.

The PPMS is capable of measuring a wide range of physical characteristics, such as magnetic susceptibility, thermal conductivity, electrical resistivity, and many more. Researchers can develop a thorough understanding of the electrical and magnetic properties of the materials under study by integrating these data with information on temperature and magnetic field dependence. The system is an effective instrument for fundamental research and the identification of unique physical processes in a variety of materials due to its adaptability, high sensitivity, and precision.

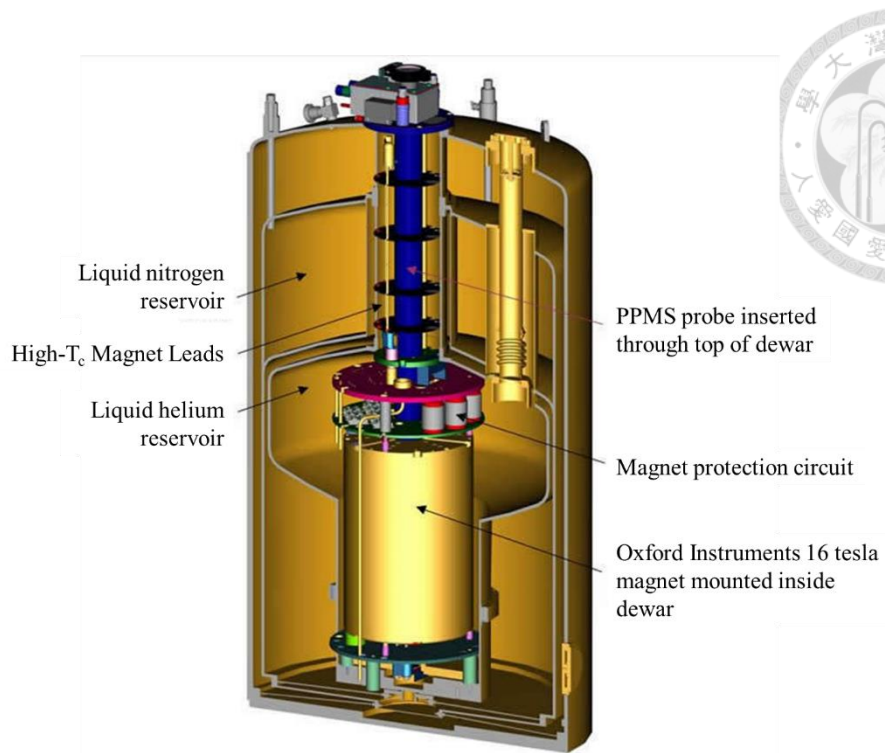


Fig. 3.12 Function of the PPMS - Quantum Design PPMS-16T.[39]

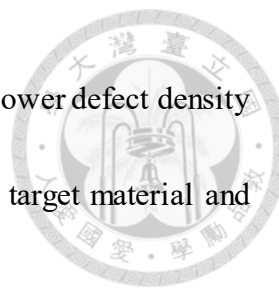
Chapter 4. Results and Discussion



4.1 Topological Thin Film Analysis

4.1.1 Scanning Electron Microscope Analysis

At the beginning of the epitaxial growth experiment, we set two parameters for adjustment: the weight of the target material and the epitaxial growth time. Referring to previous literatures[13, 21, 33, 40] on epitaxial growth and considering the melting point of Bi_2Se_3 , we chose 800°C as the center temperature of the furnace tube. Subsequently, we conducted a comparative analysis to assess the effects of different constant temperature times (1 hour, 1 hour 30 minutes, 2 hours 30 minutes, and 4 hours) and target material weights (300 mg and 600 mg) on the deposited films. This analysis is supported by the SEM images in Figure 4.1 (a)-(h). From Figure 4.1 SEM images, it is evident that the epitaxial films deposited with 600 mg target material exhibit superior surface quality compared to those with 300 mg. The 600 mg films already display the desired hexagonal crystal structure of Bi_2Se_3 . Moreover, within the 600 mg target material parameter, the length of the epitaxial time also plays a role in film quality. Films deposited for both 1 hour 30 minutes and 2 hours 30 minutes show fewer defects compared to those deposited for 1 hour and 4 hours. Specifically, when comparing the films deposited for 1 hour 30



minutes and 2 hours 30 minutes, it is evident that the latter exhibits a lower defect density than the former. Hence, the ideal configuration comprises a 600 mg target material and an epitaxial period of 2 hours 30 minutes.

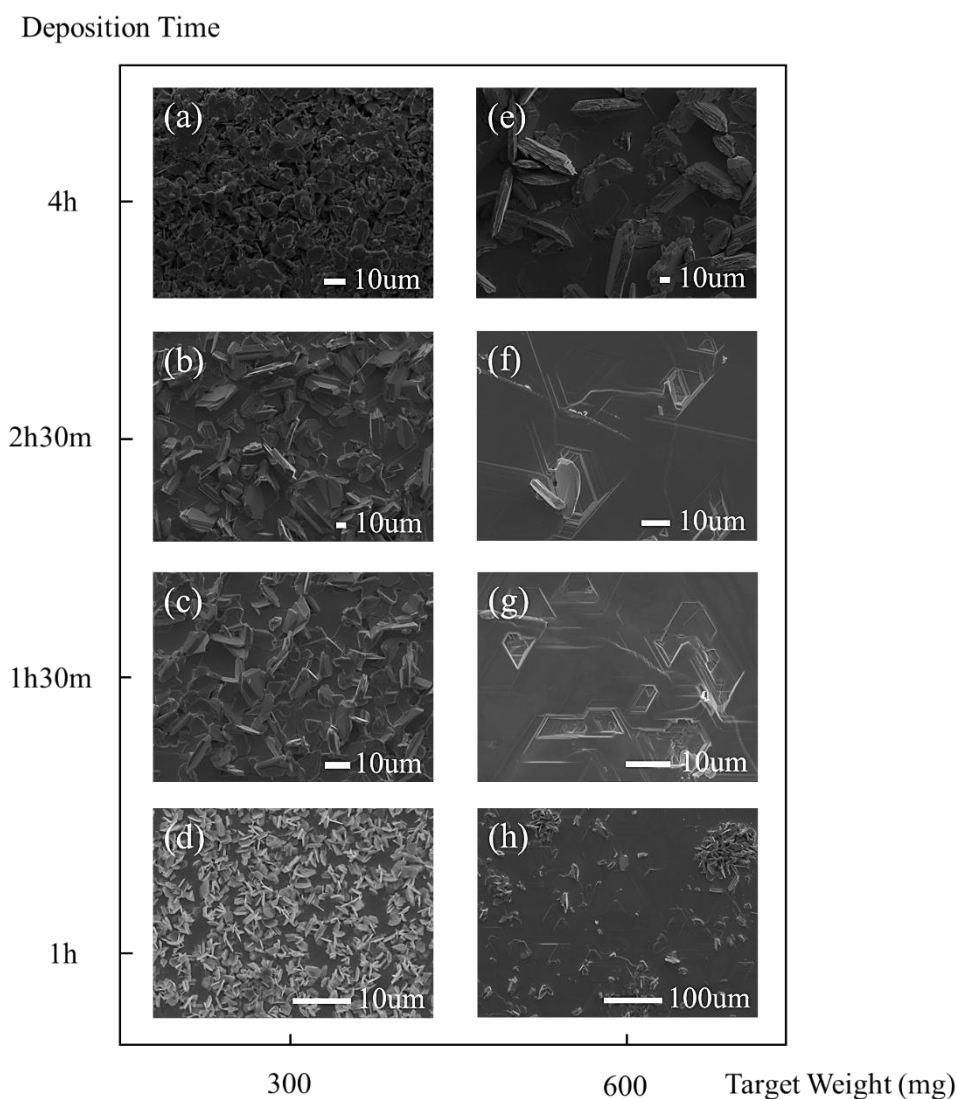


Fig. 4.1 The growth of Bi_2Se_3 on a Al_2O_3 substrate under different conditions, with target weights of 300mg (a)-(d) and 600mg (e)-(h), and deposition times of 1 hour, 1 hour 30 minutes, 2 hours 30 minutes, and 4 hours, respectively.

Although the Bi_2Se_3 thin films grown for 2 hours 30 minutes already exhibited a

hexagonal crystal structure, we introduced a second-step temperature epitaxial growth process to further improve their surface defects. The second-step temperature was set from the left to right zones of the tube furnace as 650°C, 20°C, and 650°C. The temperature ramp-up time for this step was set at 1 hour 30 minutes, followed by natural cooling. The purpose of the second-step temperature was to lower the temperature in the middle region, allowing any remaining impurities and defects to preferentially deposit in the middle region rather than on the surrounding substrates. This approach aimed to minimize the impact of defects on the film's surface and enhance its overall quality. By carefully controlling the temperature gradient, we could encourage the deposition of impurities and defects away from the substrate edges, leading to improved film properties. The initial assessment of surface smoothness was done based on visual observation with



Fig. 4.2 Photograph of (a) one-step (b) two-step Bi_2Se_3 thin film surface.

the naked eye, and Figure 4.2 shows an image captured using a mobile phone. Figure 4.2(a) depicts a Bi_2Se_3 film grown using a single-step temperature process, with crystal growth parameters of 300°C, 800°C, and 300°C maintained for 2 hours and 30 minutes. As shown in Figure 4.2 (a), preliminary visual inspection reveals a metallic silver appearance on the surface, but it does not exhibit a smooth texture. Figure 4.2(b)

illustrates a Bi_2Se_3 film grown using a two-step temperature process, with the temperature and epitaxial time for both steps being identical to those described in the previous section.

Preliminary visual inspection reveals a similar metallic silver appearance on the surface as in Figure 4.2 (a), but with a mirror-like smoothness. Therefore, upon comparing photographs Figure 4.2 (a) and (b), it is evident that the epitaxial quality in (b) surpasses that in (a). Additionally, both (a) and (b) demonstrate the complete deposition of Bi_2Se_3 on the Al_2O_3 substrate. Figure 4.3 depicts the growth morphology change of the Bi_2Se_3 film on an Al_2O_3 substrate.

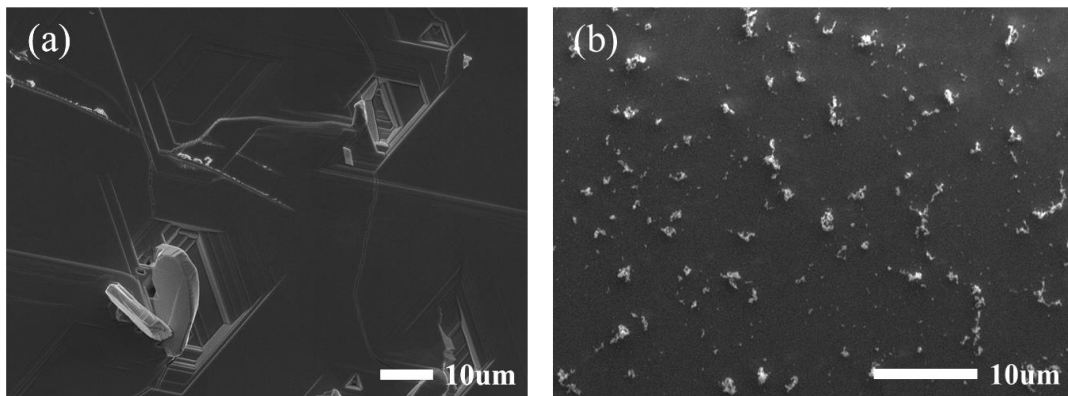
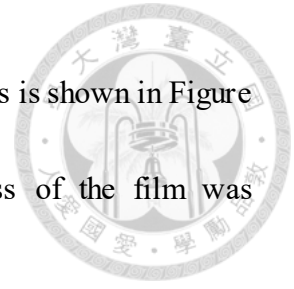


Fig. 4.3 SEM of (a)one-step (b) two-step Bi_2Se_3 thin film surface.

Figure 4.3(a) shows a generally smooth surface structure with some symmetrical triangular and hexagonal morphologies exhibiting smooth multilayer structures arranged in the same direction. On the other hand, Figure 4.3(b) shows the surface after undergoing the second-step epitaxy, gradually forming a highly smooth planar layer. On the surface, some dendritic characteristics are visible, which may be related to internal stress [18].

The cross-section scanning electron microscope (SEM) image of films is shown in Figure 3.4, which clearly depict a relatively smooth layer. The thickness of the film was estimated to be around 700 nm for deposition on Al₂O₃ substrates.



4.1.2 X-ray Photoelectron Spectroscopy Analysis



In order to determine the chemical stoichiometry of our thin films, we employed X-ray photoelectron spectroscopy (XPS) with an Al K α monochromator X-ray source. We utilized this technique to investigate the influence of the environment on Bi₂Se₃ thin films, and recorded XPS spectra for samples prepared through both one-step and two-step temperature processes. Figure 4.4 shows the full-range scan, revealing the presence of peaks corresponding to Bi, Se, O, and C. In this figure, there is not a significant difference between the samples prepared using the one-step and two-step temperature processes, so closer inspection of the Se 3d and Bi 4f spectra is necessary. Additionally, it is worth noting that the presence of trace amounts of carbon (C) and oxygen (O) during the synthesis is not uncommon [41]. This could be attributed to the adsorption of CO₂, O₂, or H₂O on the surface of the sample. This finding further supports the formation of a high-purity product in our study.

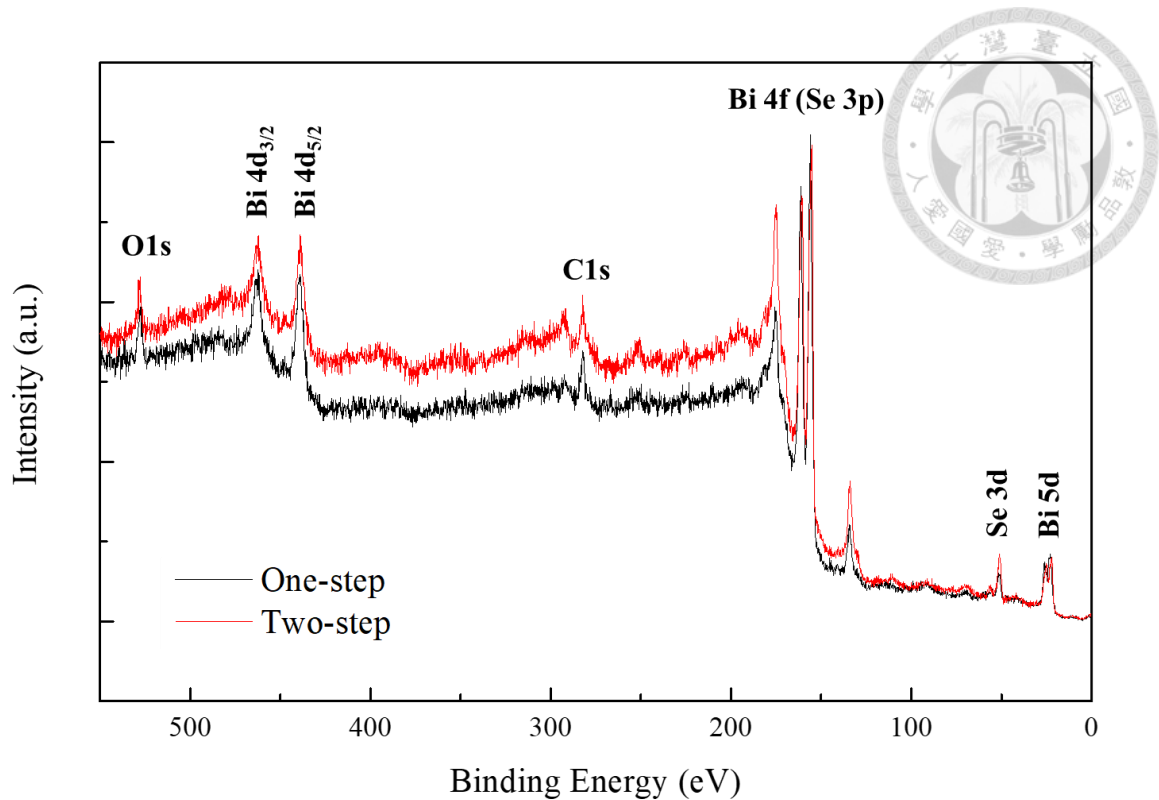


Fig. 4.4 XPS patterns of Bi_2Se_3 thin films deposited on Al_2O_3 substrates.

Figure 4.5 shows the spectrum of the sample prepared using the one-step temperature process. In Figure 4.5(a), the selenium spectrum appears as a broad peak, which can be deconvoluted into two peaks at 50.95 eV and 51.775 eV, corresponding to $\text{Se } 3d_{5/2}$ and $\text{Se } 3d_{3/2}$, respectively. Figure 4.5(b) displays the XPS spectrum of the Bi 4f core level, clearly showing two sets of spin-orbit doublet components with peak positions at approximately 156.3 eV and 161.525 eV, corresponding to $\text{Bi } 4f_{7/2}$ and $\text{Bi } 4f_{5/2}$, respectively. Although this data indicates successful fabrication of Bi_2Se_3 films, a slight deviation in binding energy is observed compared to previous research[41-43].

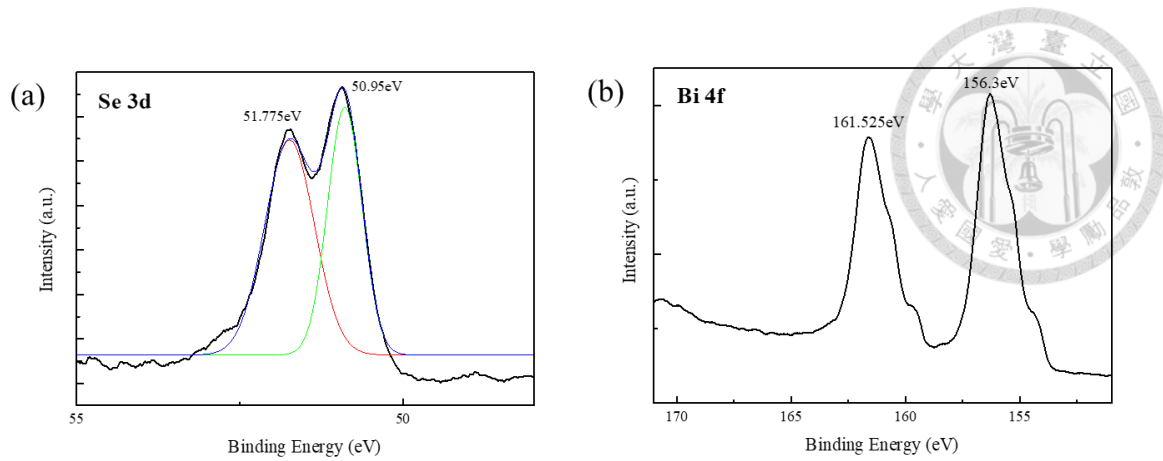


Fig. 4.5 XPS spectra of one-step Bi_2Se_3 thin film: (a) Se 3d peaks; (b) Bi 4f peaks.

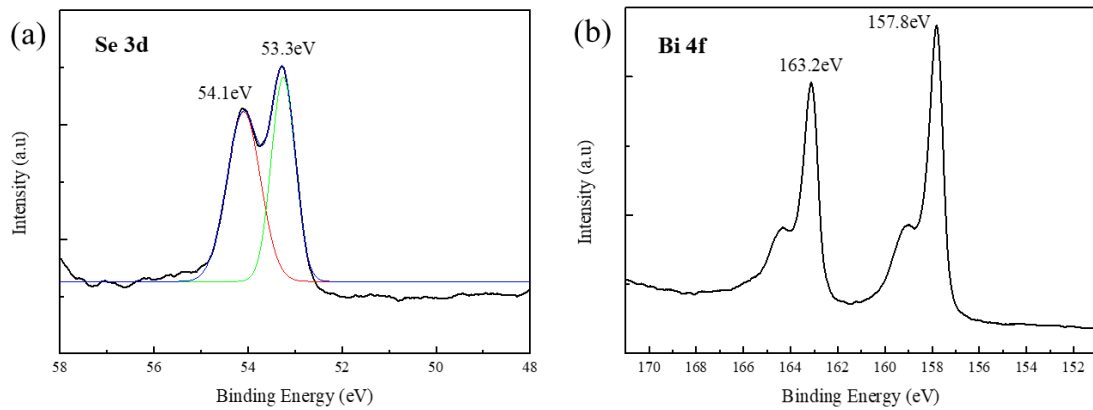


Fig. 4.6 XPS spectra of two-step Bi_2Se_3 thin film: (a) Se 3d peaks; (b) Bi 4f peaks.

Therefore, we further conducted measurements using the same approach on the samples prepared via the two-step temperature process. The Se 3d spectrum displayed in Figure 4.6(a) exhibits an excellent fit using two peaks corresponding to Se $3d_{5/2}$ and $3d_{3/2}$, with binding energies of 53.3 and 54.1 eV, respectively. This observation suggests the presence of Se in the films as a compound of Bi_2Se_3 . In Figure 4.6(b), the Bi 4f spectrum is fitted well by the Bi $4f_{7/2}$ and $4f_{5/2}$ peaks located at 157.8 and 163.2 eV, respectively. The observed energy splitting of 5.4 eV aligns with previous reports[43]. Notably, the Se $3d_{5/2}$ peak exhibits a red shift of approximately 2.2 eV compared to pure bulk Se, while

the Bi 4f peaks demonstrate a blue shift of approximately 1.1 eV[42, 44]. These opposing shifts in binding energy are attributed to the Se-Bi bonding, which involves charge transfer from Bi to Se. Thus, these findings confirm the formation of high-purity Bi₂Se₃ films in this study.

According to the XPS data, the atomic percentage can be estimated using the ratio of relative sensitivity factors (RSF) and peak area, as well as a simple algorithm suggested by previous literature[45-47]. Therefore, we derived the following formula to estimate the atomic percentage.

$$\frac{Bi}{Se} \% = \frac{\frac{Bi \text{ peak area}}{RSF_{Bi}}}{\frac{Se \text{ peak area}}{RSF_{Se}}} \times 100\%$$

Since the areas of C and O are negligible, they can be disregarded. The atomic percentages of 44.43% for Bi and 55.57% for Se can be obtained in the one-step growth of the Bi₂Se₃ thin film. The slight deviation from the theoretical ratio of Bi₂Se₃ suggests the possible presence of Se vacancies or defects. The atomic percentages of 40.86% for Bi and 59.14% for Se can be obtained in the two-step growth. The atomic ratio of Bi and Se is close to the theoretical ratio of Bi₂Se₃, indicating the phase purity and high crystalline quality of the two-step grown sample.



4.1.3 X-ray Diffraction Analysis

To gain a deeper understanding of the crystal structure of materials, we employ X-ray diffraction (XRD) measurements with Cu-K α radiation source. Therefore, by analyzing XRD patterns, we can determine the crystalline nature and phase purity of the Bi₂Se₃ thin films prepared using a tube furnace. In Figure 4.7, we present high-resolution XRD 2 θ -omega scans of the Bi₂Se₃ thin film deposited through a one-step temperature process on an Al₂O₃ substrate (Figure 4.7(a)) and a two-step temperature process (Figure 4.7(b)). These scans were conducted in the angular range of 2 θ_{\min} = 5° to 2 θ_{\max} = 90°. As shown in Figure 4.7, several diffraction peaks appear at approximately 9.3°, 18.6°, 28.1°, 37.8°, 47.7°, 58.1°, and 68.9°, corresponding to the (0003), (0006), (0009), (0012), (0015), (0018), and (0021) planes of hexagonal Bi₂Se₃, respectively. These diffraction peaks indicate that the material possesses the same rhombohedral layered crystal structure as pure Bi₂Se₃ and belongs to the $R\bar{3}m$ space group[48]. In the case of the film deposited on the Al₂O₃ (0001) substrate, only the 0003n family related to hexagonal Bi₂Se₃ and the Al₂O₃ substrate peaks were observed. This observation confirms the presence of highly c-axis-oriented Bi₂Se₃ thin films on the Al₂O₃ substrate. Furthermore, Figure 4.7 reveals that the lattice spectrum of the Bi₂Se₃ thin film deposited using the two-step method is significantly superior to that of the film deposited using the one-step method. Specifically,

for the Bi_2Se_3 (0006) plane, a higher intensity and sharper peak were observed in Figure 4.8(b) compared to Figure 4.8(a) at the same intensity scale. From the XRD data, the (0006) plane peaks were analyzed by fitting them with Gaussian functions. The obtained full width at half maximum (FWHM) values for the (0006) peak were found to decrease from 0.22 to 0.09 for the one-step and two-step processes, respectively. These findings indicate that the crystallinity of the Bi_2Se_3 thin film improves with the inclusion of the second temperature step, as evidenced by the increased intensity and decreased FWHM of the diffraction peaks.

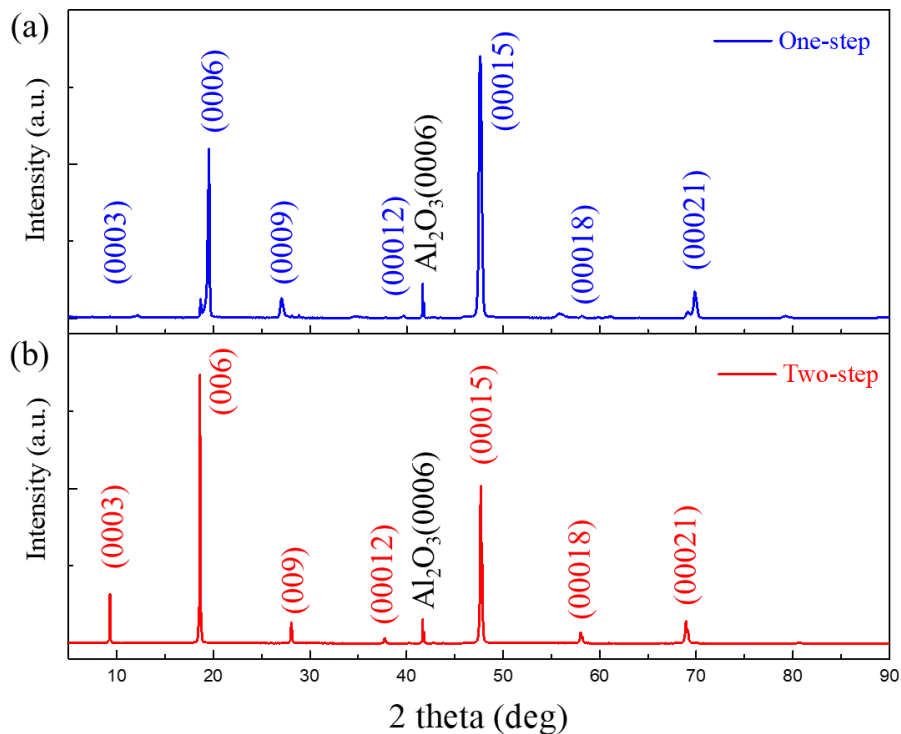


Fig. 4.7 XRD patterns of Bi_2Se_3 films deposited on Al_2O_3 substrates, (a) one-step growth, (b) two-step temperature growth.

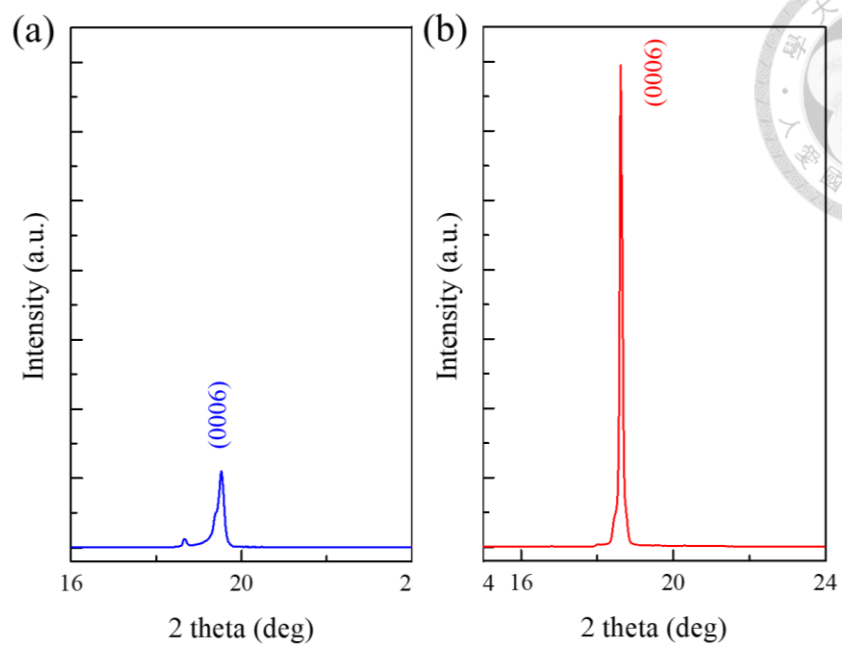


Fig. 4.8 XRD patterns of Bi_2Se_3 (0006) peak, (a) one-step growth, (b) two-step growth.

4.2 Magnetotransport of Topological Material



In this chapter, we employed a two-step epitaxial growth technique to fabricate Bi_2Se_3 thin films on Al_2O_3 substrates. On the films, electrodes were then fabricated. In the study of transport properties in Bi_2Se_3 topological insulator films, it is crucial to differentiate between surface-state and bulk-state transport. A commonly used method to determine whether the transport is dominated by surface states or bulk states is through applied magnetic field measurements. Therefore, in this experiment, we conducted magnetotransport measurements using the Quantum Design Physical Property Measurement System-16T system.

As shown in Figures 4.9, the resistance of the Bi_2Se_3 thin film decreases with decreasing temperature, and gradually saturates at the temperature around 30K. In topological insulator thin films, lattice defects serve as carriers introduced by doping. Therefore, from Figures 4.9, we can observe that the resistance of the two-step temperature-grown film is higher than that of the one-step film. In the case of the one-step thin film, impurities replace certain atoms, introducing additional free carriers or defect states[49, 50]. These free carriers or defect states facilitate the movement of electrons within the material, consequently enhancing its conductivity. In the case of Bi_2Se_3 , naturally formed selenium vacancies fill the conduction band, resulting in a

metallic behavior of the film. Furthermore, the presence of these naturally occurring defects shifts the Fermi level towards the bulk conduction band, leading to an n-type behavior of the system[51], consistent with the bulk carrier concentration results obtained from Hall measurements for both one-step (-1.8×10^{19}) and two-step (-4.36×10^{18}) growth thin films. Additionally, the unique band structure of Bi_2Se_3 thin films includes not only a bulk conduction band but also surface states. These surface states intersect with the Fermi level. This particular band structure is a unique feature of topological materials [3, 52], as shown in the inset of Figures 4.9 (a).

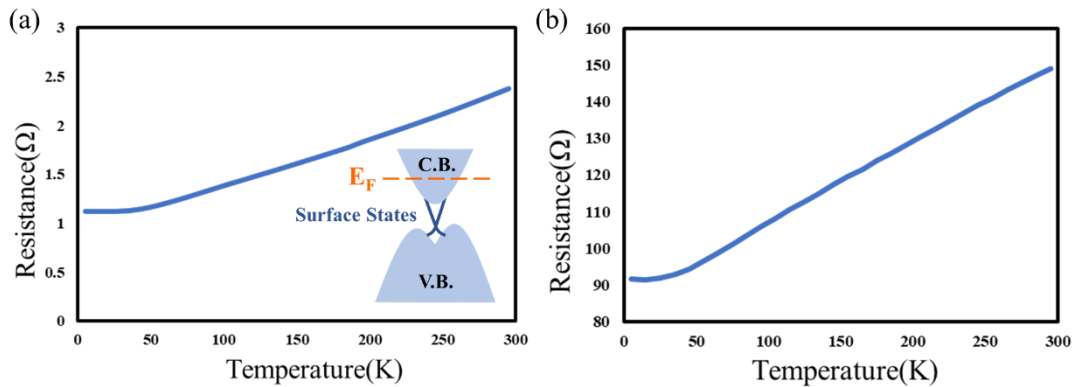
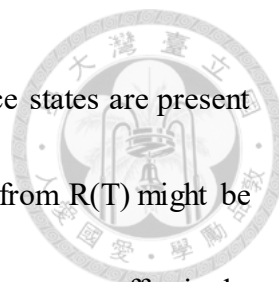


Fig. 4.9 Resistance vs temperature curves taken from 5 to 300 K: (a) one-step growth, (b) two-step growth.

It's important to note that the resistance-temperature curve ($R(T)$) of the two-step growth film exhibits a higher slope compared to that of the one-step growth film. However, in the case of Bi_2Se_3 films, when both bulk and surface states coexist, the dominant influence of the bulk states might completely mask the contribution of the



surface states to the $R(T)$. In other words, when both bulk and surface states are present within the film, accurately distinguishing the effects of surface states from $R(T)$ might be challenging due to the potentially stronger impact of the bulk states, effectively overshadowing the contribution of surface states.

This implies that the difference in $R(T)$ slopes primarily arises from the variations in bulk carrier mobility and concentration with temperature. These changes are influenced by the intrinsic quality of the film's internal structure. In other words, the presence of impurities within the film could directly alter the bulk carrier mobility and concentration, consequently leading to a reduced slope in the $R(T)$ curve. This reduction reflects a decreased sensitivity of the film's resistance to temperature variations.

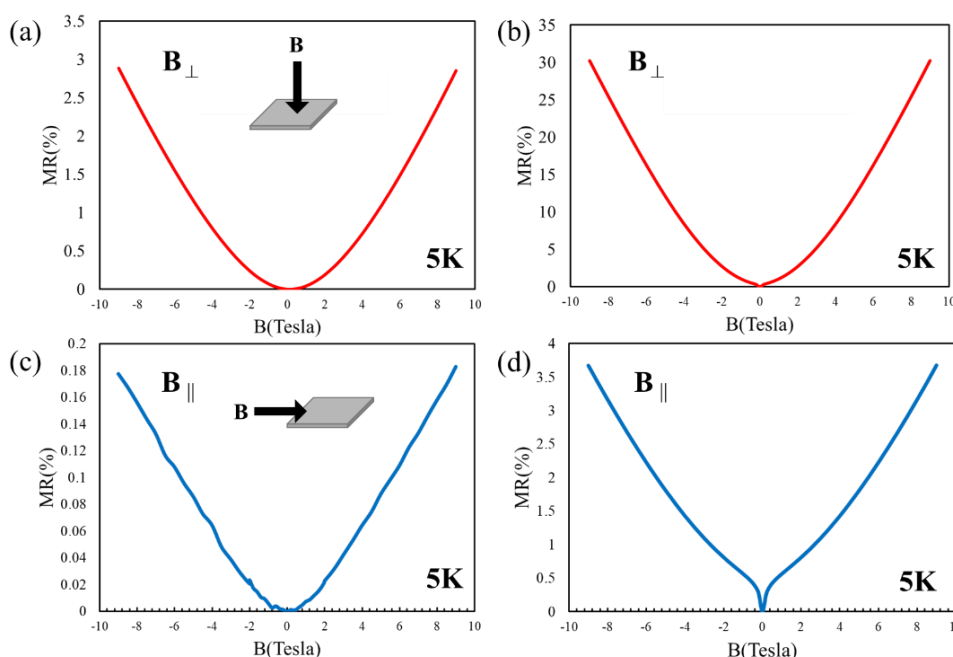
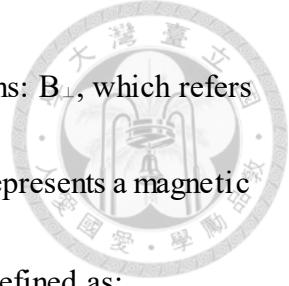


Fig. 4.10 Perpendicular MR for the film at 5 K: (a) one-step growth, (b) two-step growth.

Parallel MR for the film at 5 K: (c) one-step growth, (d) two-step growth.



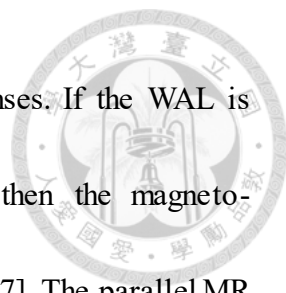
Subsequently, we employ two distinct magnetic-field orientations: B_{\perp} , which refers to a magnetic field perpendicular to the film surface, and B_{\parallel} , which represents a magnetic field parallel to the sample surface. The magnetoresistance (MR) is defined as:

$$\text{MR} = \frac{R(B) - R(0)}{R(0)} \times 100\%$$

where $R(B)$ denotes the resistance under a magnetic field and $R(0)$ represents the resistance at zero magnetic field.

Figure 4.10 illustrates the anisotropic MR behavior[52-55]. The perpendicular MR is greater than the parallel MR at 5K, indicating that the transport of topological insulators is sensitive to B_{\perp} . A sharp cusp is clearly observed at $T=5\text{K}$, indicating the presence of a weak antilocalization (WAL) effect. It can be observed that the WAL effect is more pronounced in the two-step grown thin films compared to the one-step grown thin films. This is because the WAL effect arises from coherent scattering due to the electron's motion in the material, influenced by spin-orbit coupling and electron-electron interactions. When the defect density is lower, scattering events are reduced, thereby enhancing the manifestation of the WAL effect.

Additionally, the perpendicular MR induced by high magnetic fields shows a linear and non-saturating behavior, suggesting that our topological insulator film exhibits two-dimensional characteristics[52, 56]. The two-dimensional characteristics in topological insulators stem from special surface states that confine electrons to predominantly move



within the material's surface, resulting in magnetoresistance responses. If the WAL is primarily caused by spin-orbit coupling in a 3D bulk channel, then the magnetoconductivity should be independent of the magnetic field tilt angles[57]. The parallel MR of the film, as shown in Figure 4.10 (c) and (d), follows an approximately parabolic B-field dependence over the entire range of magnetic fields. This semiclassical B² dependence results from the Lorentz deflection of carriers. According to Kohler's rule:

$$\frac{R(B)}{R(0)} \approx 1 + (\mu B)^2$$

where μ represents the thin film mobility. The mobility (μ) is greater in the direction of the magnetic field perpendicular to the film compared to the direction of the magnetic field parallel to the film. As a result, the influence of the Lorentz force is more pronounced in the case of a perpendicular magnetic field, leading to significant deflection in the trajectories of charge carriers. On the other hand, in the case of a magnetic field parallel to the film, the impact of the Lorentz force is relatively smaller, resulting in less significant deflection of charge carrier trajectories. Due to the stronger influence of the Lorentz force on charge carriers in the perpendicular magnetic field, the changes in thin film resistivity in this direction are more apparent. Conversely, in the direction of the parallel magnetic field, the MR effect is less pronounced. In other words, topological materials possess surface states with strong spin-orbit coupling, making them highly sensitive to external magnetic fields. The surface states of the material are directly

influenced by the magnetic field lines in a perpendicular magnetic field, which causes a more noticeable fluctuation in resistivity when a perpendicular magnetic field is applied.

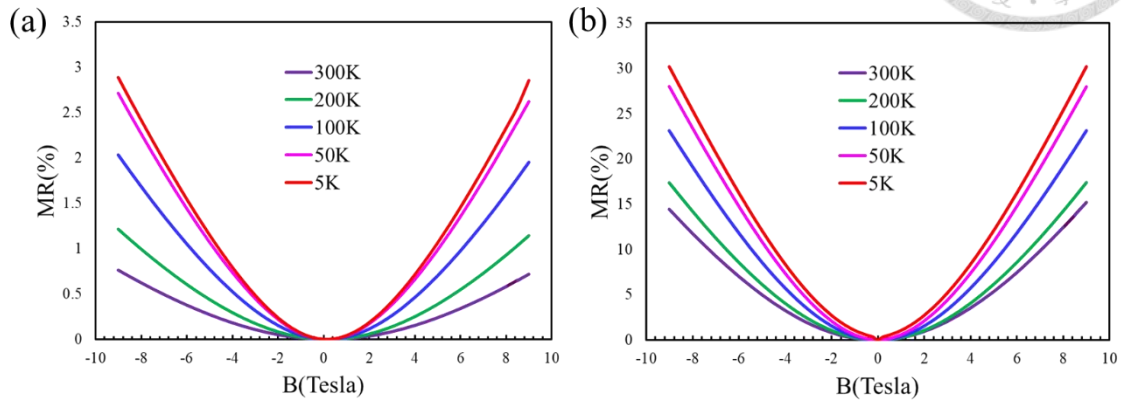
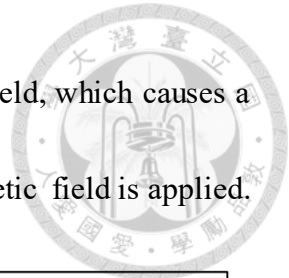



Fig. 4.11 MR of thin film at different temperatures: (a) one-step growth, (b) two-step growth.

Further MR measurements were performed under a perpendicular magnetic field in the temperature range of 5 to 300 K and magnetic field strength from -9 to 9 T. The MR increases with the magnetic field, which agree with the typical observation of topological insulators in the presence of an external magnetic field [58].

For both one-step and two-step grown Bi_2Se_3 films, we have observed a temperature-dependent linear MR (LMR) effect, as illustrated in Figure 4.11. This LMR effect is characterized by a linear change in the sample's resistance with increasing magnetic field. Such behavior can be attributed to either quantum[59] or classical[60] mechanisms, which are known to cause LMR in various materials.

Despite the differences in MR values, the temperature and magnetic field



dependence of the LMR effect are remarkably similar between the one-step and two-step produced Bi_2Se_3 thin films. Both show a V-shaped cusp at low temperatures and low magnetic fields, a phenomenon often associated with the WAL effect observed in various topological materials. As the temperature increases, the MR decreases and exhibits a trend consistent with classical quadratic field dependence at higher temperatures. Additionally, the LMR effect becomes less temperature-dependent below 50 K, and the high-field MR deviates from the quadratic curve, indicating a tendency towards linear behavior.

Furthermore, a notable finding was that the MR values obtained from the one-step growth of the Bi_2Se_3 thin film were consistently smaller compared to the MR values from the two-step growth. This difference suggests that the one-step growth sample may possess a more distinct conductive channel due to the presence of impurity doping, which helps form and enhance the conductive channels for electron transport, thereby leading to the observation of a smaller MR. On the other hand, the relatively larger MR in the two-step growth sample could be attributed to the improved crystalline quality and reduced defects resulting from the second-step growth process, leading to the observation of a larger MR.

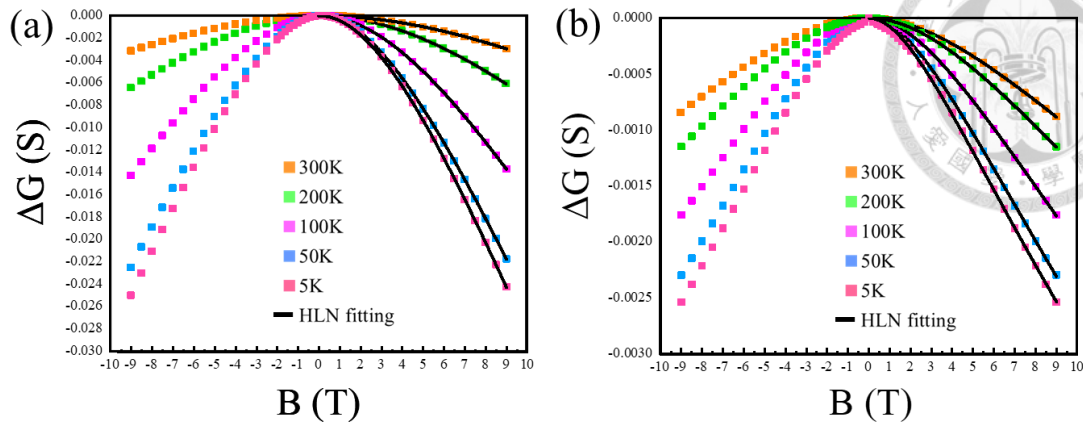
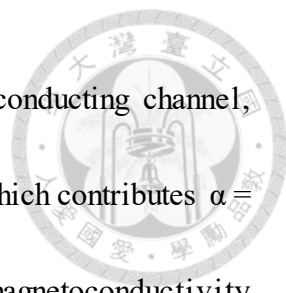


Fig. 4.12 Magnetoconductance analysis of Bi_2Se_3 single crystal measured at different temperatures: (a) one-step growth, (b) two-step growth. The black solid line represents the HLN fitting.

In addition, the magnetoconductance of the crystal is analyzed in order to investigate the role of surface and bulk carriers at various temperatures and magnetic fields, as shown in Fig. 9. The magnetoconductance exhibits a sharp cusp at low magnetic fields and temperatures, which broadened with increasing temperature. The contribution of WAL in magnetoconductance, $\Delta G = G(B) - G(B = 0)$, arising from the Dirac-like surface states in 3D topological insulators, can be analyzed using the following Hikami-Larkin-Nagaoka (HLN equation) [30, 32, 61, 62]:

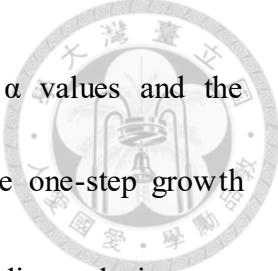
$$\Delta G(B) = G(B) - G(0) = -\frac{\alpha e^2}{\pi h} \left[\ln\left(\frac{B_\phi}{B}\right) - \psi\left(\frac{1}{2} + \frac{B_\phi}{B}\right) \right]$$

where, e is the electronic charge, h is the Plank's constant, B is the applied magnetic field, ψ is the digamma function, $B_\phi = \frac{h}{8e\pi L_\phi^2}$ is the characteristic magnetic field, and L_ϕ and α are the two fitting parameters signifying phase coherence length and prefactor



respectively. In a topological insulator, $\alpha = -1/2$ represents a single conducting channel, whereas $\alpha = -1$ denotes two separate conducting channels, each of which contributes $\alpha = -1/2$ [12]. The HLN model was originally introduced to describe the magnetoconductivity σ in ideal two-dimensional spin-orbit coupled systems, considering only the contribution of surface states in 3D topological insulators. It can also be applied to thin films to simplify the analysis and circumvent the complexity of considering bulk states. Importantly, the HLN model continues to be utilized for analyzing the magnetoconductance of thick films of 3D topological insulators, even as the sample thickness increases [29, 57, 62, 63].

Through HLN fitting analysis of our magnetoconductance data, as shown in Fig. 9, we observed that as the temperature increases from 5 K to 300 K, the L_ϕ of the one-step growth film decreases from 6.228 nm to 4.128 nm, while the L_ϕ of the two-step growth film decreases from 9.242 nm to 6.246 nm. This temperature dependence could be attributed to inelastic electron-phonon or electron-electron scattering [64]. From the data fitting, we found that the α values for the one-step growth film ($\alpha \sim -1.5 \times 10^4$) and the two-step growth film ($\alpha \sim -6.6 \times 10^2$) are significantly higher than the typical range, consistent with results reported for other 3D topological insulator samples with similar sample thicknesses [29, 57, 62]. The pronounced increase in α values may primarily be influenced by the presence of the 3D bulk channel. Through analysis of the fitting



parameters, we observed a correlation between the increase in α values and the corresponding decrease in L_φ values. This suggests that during the one-step growth process, impurity defects may form additional conduction channels leading to the increase in α values, stated differently, a smaller α value indicates a more prominent contribution from the surface conduction channel. However, these additional conduction channels exhibit relatively weaker phase coherence compared to the stability of surface states. Therefore, our fitting results indicate that in the case of two-step growth, the L_φ value remains larger than in the one-step growth scenario, implying a relatively diminished influence of impurity scattering.

Through temperature-dependent measurements, it is evident that with increasing temperature, the contribution from bulk states dominates the overall electrical conductivity, further confirming the significance of 3D bulk channels in the thick film samples of 3D topological insulators.


Chapter 5. Conclusion



In this study, we successfully compared the deposition of Bi_2Se_3 thin films on Al_2O_3 substrates using one-step and two-step epitaxial growth techniques. Through comprehensive analysis using various characterization techniques, it was observed that the two-step temperature deposition method significantly improved the quality of Bi_2Se_3 films. This improvement was confirmed through initial visual inspection, SEM images, and XRD patterns, which revealed that films deposited using the two-step temperature approach exhibited better crystallinity and surface smoothness. The enhanced quality can be attributed to the temperature setting in the second step, which effectively reduced surface defects and improved the film's crystalline quality.

Furthermore, XPS analysis indicated that the two-step temperature deposition method effectively controlled the chemical composition of the Bi_2Se_3 film. This result suggested that the temperature setting in the second step contributed to adjusting the distribution and chemical bonding of elements in the film, further enhancing its performance and stability. Therefore, by further optimizing deposition conditions and adjusting parameters such as the temperature and deposition rate in the second step, the crystallinity and interface properties of the film can be further improved. These insights provide valuable guidance for the future design and manufacturing of high-performance

Bi₂Se₃ thin films.



Additionally, we utilized the PPMS to investigate the magnetotransport of films fabricated using both one-step and two-step epitaxial growth methods. By comparing the magnetotransport behaviors of these films, we gained a deeper understanding of their response to external magnetic fields and transport properties. The one-step epitaxial growth exhibited clear indications of impurities in both the resistance-temperature relationship and the MR performance. In contrast, the two-step epitaxial growth demonstrated more pronounced characteristics of a topological insulator, showing a more significant WAL effect, higher MR values, and greater sensitivity to external magnetic fields. Furthermore, the fitting using the HLN equation revealed that our epitaxial thin films, due to their relatively larger thickness, exhibited a significant contribution from bulk-state transport. Moreover, the observed smaller value of α in the two-step growth compared to the one-step growth suggests a more prominent two-dimensional characteristic, indicating a better topological material.

In conclusion, our research findings confirm that adopting the two-step temperature deposition method significantly improves the quality and enhances the topological characteristics of Bi₂Se₃ thin films on Al₂O₃ substrates. This has important implications for the development and application of thermoelectric materials and magnetic sensors, while also providing valuable references and insights for related research fields.



Reference

- [1] H. Peng *et al.*, "Aharonov–Bohm interference in topological insulator nanoribbons," *Nature Materials*, vol. 9, no. 3, pp. 225-229, 2010/03/01 2010, doi: 10.1038/nmat2609.
- [2] J. Chen *et al.*, "Gate-Voltage Control of Chemical Potential and Weak Antilocalization in $\{\mathrm{Bi}\}_{2}\{\mathrm{Se}\}_{3}$," *Physical Review Letters*, vol. 105, no. 17, p. 176602, 10/19/ 2010, doi: 10.1103/PhysRevLett.105.176602.
- [3] H.-T. He *et al.*, "Impurity Effect on Weak Antilocalization in the Topological Insulator $\{\mathrm{Bi}\}_{2}\{\mathrm{Te}\}_{3}$," *Physical Review Letters*, vol. 106, no. 16, p. 166805, 04/21/ 2011, doi: 10.1103/PhysRevLett.106.166805.
- [4] J. G. Checkelsky, Y. S. Hor, R. J. Cava, and N. P. Ong, "Bulk band gap and surface state conduction observed in voltage-tuned crystals of the topological insulator $\mathrm{Bi}_2\mathrm{Se}_3$," *Phys Rev Lett*, vol. 106, no. 19, p. 196801, May 13 2011, doi: 10.1103/PhysRevLett.106.196801.
- [5] D.-X. Qu, Y. S. Hor, J. Xiong, R. J. Cava, and N. P. Ong, "Quantum Oscillations and Hall Anomaly of Surface States in the Topological Insulator $\mathrm{Bi}_2\mathrm{Te}_3$," *Science*, vol. 329, no. 5993, pp. 821-824, 2010, doi: doi:10.1126/science.1189792.
- [6] Z. Ren, A. A. Taskin, S. Sasaki, K. Segawa, and Y. Ando, "Large bulk resistivity and surface quantum oscillations in the topological insulator $\{\mathrm{Bi}\}_{2}\{\mathrm{Te}\}_{2}\{\mathrm{Se}\}$," *Physical Review B*, vol. 82, no. 24, p. 241306, 12/09/ 2010, doi: 10.1103/PhysRevB.82.241306.
- [7] W. Richter and C. R. Becker, "A Raman and far-infrared investigation of phonons in the rhombohedral V2–VI3 compounds $\mathrm{Bi}_2\mathrm{Te}_3$, $\mathrm{Bi}_2\mathrm{Se}_3$, $\mathrm{Sb}_2\mathrm{Te}_3$ and $\mathrm{Bi}_2(\mathrm{Te}_{1-x}\mathrm{Se}_x)_3$ ($0 < x < 1$), $(\mathrm{Bi}_{1-y}\mathrm{Sb}_y)_2\mathrm{Te}_3$ ($0 < y < 1$)," *Physica Status Solidi (b)*, vol. 84, no. 2, pp. 619-628, 1977, doi: 10.1002/pssb.2220840226.
- [8] Y. L. Chen *et al.*, "Experimental realization of a three-dimensional topological insulator, $\mathrm{Bi}_2\mathrm{Te}_3$," (in eng), *Science*, vol. 325, no. 5937, pp. 178-81, Jul 10 2009, doi: 10.1126/science.1173034.
- [9] H. Zhang, C.-X. Liu, X.-L. Qi, X. Dai, Z. Fang, and S.-C. Zhang, "Topological insulators in $\mathrm{Bi}_2\mathrm{Se}_3$, $\mathrm{Bi}_2\mathrm{Te}_3$ and $\mathrm{Sb}_2\mathrm{Te}_3$ with a single Dirac cone on the surface," *Nature Physics*, vol. 5, no. 6, pp. 438-442, 2009/06/01 2009, doi: 10.1038/nphys1270.
- [10] N. S. Patil, A. M. Sargar, S. R. Mane, and P. N. Bhosale, "Growth mechanism and

- characterisation of chemically grown Sb doped Bi₂Se₃ thin films," *Applied Surface Science*, vol. 254, no. 16, pp. 5261-5265, 2008/06/15/ 2008, doi: <https://doi.org/10.1016/j.apsusc.2008.02.084>.
- [11] P. H. Le, C.-N. Liao, C. W. Luo, J.-Y. Lin, and J. Leu, "Thermoelectric properties of bismuth-selenide films with controlled morphology and texture grown using pulsed laser deposition," *Applied Surface Science*, vol. 285, pp. 657-663, 2013/11/15/ 2013, doi: <https://doi.org/10.1016/j.apsusc.2013.08.107>.
- [12] R. Gracia-Abad, S. Sangiao, C. Bigi, S. Kumar Chaluvadi, P. Orgiani, and J. M. De Teresa, "Omnipresence of Weak Antilocalization (WAL) in Bi(2)Se(3) Thin Films: A Review on Its Origin," *Nanomaterials (Basel)*, vol. 11, no. 5, Apr 22 2021, doi: 10.3390/nano11051077.
- [13] C.-Z. Chang *et al.*, "GROWTH OF QUANTUM WELL FILMS OF TOPOLOGICAL INSULATOR Bi₂Se₃ ON INSULATING SUBSTRATE," *SPIN*, vol. 01, no. 01, pp. 21-25, 2011/06/01 2011, doi: 10.1142/S2010324711000033.
- [14] P. Tabor, C. Keenan, D. Lederman, and S. Urazhdin, "Growth of the topological insulator Bi₂Se₃ on Al₂O₃ by molecular beam epitaxy," 03/01 2011.
- [15] S. Huang *et al.*, "Fracture Behavior of Single-Crystal Sapphire in Different Crystal Orientations," *Crystals*, vol. 11, no. 8, p. 930, 2021. [Online]. Available: <https://www.mdpi.com/2073-4352/11/8/930>.
- [16] A. Ambrosi, Z. Sofer, J. Luxa, and M. Pumera, "Exfoliation of Layered Topological Insulators Bi₂Se₃ and Bi₂Te₃ via Electrochemistry," *ACS Nano*, vol. 10, no. 12, pp. 11442-11448, 2016/12/27 2016, doi: 10.1021/acsnano.6b07096.
- [17] N. H. Tu *et al.*, "Large-Area and Transferred High-Quality Three-Dimensional Topological Insulator Bi_{2-x}SbxTe_{3-y}Se_y Ultrathin Film by Catalyst-Free Physical Vapor Deposition," *Nano Letters*, vol. 17, no. 4, pp. 2354-2360, 2017/04/12 2017, doi: 10.1021/acs.nanolett.6b05260.
- [18] L. D. Alegria *et al.*, "Structural and Electrical Characterization of Bi₂Se₃ Nanostructures Grown by Metal-Organic Chemical Vapor Deposition," *Nano Letters*, vol. 12, no. 9, pp. 4711-4714, 2012/09/12 2012, doi: 10.1021/nl302108r.
- [19] X. Chen, X. C. Ma, K. He, J. F. Jia, and Q. K. Xue, "Molecular beam epitaxial growth of topological insulators," *Adv Mater*, vol. 23, no. 9, pp. 1162-5, Mar 4 2011, doi: 10.1002/adma.201003855.
- [20] S. Roy, S. Manna, C. Mitra, and B. Pal, "Photothermal Control of Helicity-Dependent Current in Epitaxial Sb₂Te₂Se Topological Insulator Thin-Films at Ambient Temperature," *ACS Applied Materials & Interfaces*, vol. 14, no. 7, pp. 9909-9916, 2022/02/23 2022, doi: 10.1021/acsaami.1c24461.
- [21] M. Liu, F. Y. Liu, B. Y. Man, D. Bi, and X. Y. Xu, "Multi-layered nanostructure Bi₂Se₃ grown by chemical vapor deposition in selenium-rich atmosphere,"

- Applied Surface Science*, vol. 317, pp. 257-261, 2014/10/30/ 2014, doi: <https://doi.org/10.1016/j.apsusc.2014.08.103>.
- [22] S. E. Harrison, S. Li, Y. Huo, B. Zhou, Y. L. Chen, and J. S. Harris, "Two-step growth of high quality Bi₂Te₃ thin films on Al₂O₃ (0001) by molecular beam epitaxy," *Applied Physics Letters*, vol. 102, no. 17, 2013, doi: 10.1063/1.4803717.
- [23] K. Ueda, Y. Hadate, K. Suzuki, and H. Asano, "Fabrication of high-quality epitaxial Bi_{1-x}Sb_x films by two-step growth using molecular beam epitaxy," *Thin Solid Films*, vol. 713, p. 138361, 2020/11/01/ 2020, doi: <https://doi.org/10.1016/j.tsf.2020.138361>.
- [24] Z. J. Yue, X. L. Wang, and S. X. Dou, "Angular-dependences of giant in-plane and interlayer magnetoresistances in Bi₂Te₃ bulk single crystals," *Applied Physics Letters*, vol. 101, no. 15, 2012, doi: 10.1063/1.4756941.
- [25] S. Barua, K. P. Rajeev, and A. K. Gupta, "Evidence for topological surface states in metallic single crystals of Bi₂Te₃," *Journal of Physics: Condensed Matter*, vol. 27, no. 1, p. 015601, 2014/12/03 2015, doi: 10.1088/0953-8984/27/1/015601.
- [26] H. T. He *et al.*, "Disorder-induced linear magnetoresistance in (221) topological insulator Bi₂Se₃ films," *Applied Physics Letters*, vol. 103, no. 3, 2013, doi: 10.1063/1.4816078.
- [27] W. J. Wang, K. H. Gao, Q. L. Li, and Z.-Q. Li, "Disorder-dominated linear magnetoresistance in topological insulator Bi₂Se₃ thin films," *Applied Physics Letters*, vol. 111, no. 23, 2017, doi: 10.1063/1.5000880.
- [28] B. A. Assaf, T. Cardinal, P. Wei, F. Katmis, J. S. Moodera, and D. Heiman, "Linear magnetoresistance in topological insulator thin films: Quantum phase coherence effects at high temperatures," *Applied Physics Letters*, vol. 102, no. 1, 2013, doi: 10.1063/1.4773207.
- [29] J. G. Checkelsky, Y. S. Hor, M. H. Liu, D. X. Qu, R. J. Cava, and N. P. Ong, "Quantum Interference in Macroscopic Crystals of Nonmetallic Bi_2Se_3 ," *Physical Review Letters*, vol. 103, no. 24, p. 246601, 12/11/ 2009, doi: 10.1103/PhysRevLett.103.246601.
- [30] A. A. Taskin, S. Sasaki, K. Segawa, and Y. Ando, "Manifestation of Topological Protection in Transport Properties of Epitaxial Bi_2Se_3 Thin Films," *Physical Review Letters*, vol. 109, no. 6, p. 066803, 08/09/ 2012, doi: 10.1103/PhysRevLett.109.066803.
- [31] L. Bao *et al.*, "Weak Anti-localization and Quantum Oscillations of Surface States in Topological Insulator Bi₂Se₂Te," *Scientific Reports*, vol. 2, no. 1, p. 726, 2012/10/11 2012, doi: 10.1038/srep00726.
- [32] S. Hikami, A. I. Larkin, and Y. Nagaoka, "Spin-Orbit Interaction and Magnetoresistance in the Two Dimensional Random System," *Progress of*

- Theoretical Physics*, vol. 63, no. 2, pp. 707-710, 1980, doi: 10.1143/PTP.63.707.
- [33] H. SHARMA and Y. C. SHARMA, "EXPERIMENTAL INVESTIGATION OF ELECTRICAL PROPERTIES OF BISMUTH SELENIDE THIN FILMS," *Chalcogenide Letters*, vol. 17, pp. 173 - 177, 2020.
- [34] G. F. Harrington and J. Santiso, "Back-to-Basics tutorial: X-ray diffraction of thin films," *Journal of Electroceramics*, vol. 47, no. 4, pp. 141-163, 2021/12/01 2021, doi: 10.1007/s10832-021-00263-6.
- [35] D. Regonini, "Anodised TiO₂ Nanotubes: Synthesis, Growth Mechanism and Thermal Stability," 2008.
- [36] K. Akhtar, S. A. Khan, S. B. Khan, and A. M. Asiri, "Scanning Electron Microscopy: Principle and Applications in Nanomaterials Characterization," in *Handbook of Materials Characterization*, 2018, ch. Chapter 4, pp. 113-145.
- [37] H. Xiao, *Introduction to Semiconductor Technology (Photolithography)*. SPIE, 2012.
- [38] A. Bashir, T. I. Awan, A. Tehseen, M. B. Tahir, and M. Ijaz, "Interfaces and surfaces," in *Chemistry of Nanomaterials*, 2020, pp. 51-87.
- [39] "National Cheng Kung University Core Facility Center machine equipment." <https://ctrmost-cfc.ncku.edu.tw/p/404-1210-7410.php?Lang=zh-tw> (accessed).
- [40] Y.-C. Lin *et al.*, "A study on the epitaxial Bi₂Se₃ thin film grown by vapor phase epitaxy," *AIP Advances*, vol. 6, no. 6, 2016, doi: 10.1063/1.4954735.
- [41] X. Yang, X. Wang, and Z. Zhang, "Synthesis and optical properties of single-crystalline bismuth selenide nanorods via a convenient route," *Journal of Crystal Growth*, vol. 276, no. 3-4, pp. 566-570, 2005, doi: 10.1016/j.jcrysgro.2004.11.422.
- [42] P. H. Le, K. H. Wu, C. W. Luo, and J. Leu, "Growth and characterization of topological insulator Bi₂Se₃ thin films on SrTiO₃ using pulsed laser deposition," *Thin Solid Films*, vol. 534, pp. 659-665, 2013/05/01/ 2013, doi: <https://doi.org/10.1016/j.tsf.2013.01.104>.
- [43] G. Zhang *et al.*, "Quintuple-layer epitaxy of thin films of topological insulator Bi₂Se₃," *Applied Physics Letters*, vol. 95, no. 5, 2009, doi: 10.1063/1.3200237.
- [44] J. H. Jeon, W. J. Jang, J. K. Yoon, and S. J. Kahng, "Metal-supported high crystalline Bi(2)Se(3) quintuple layers," *Nanotechnology*, vol. 22, no. 46, p. 465602, Nov 18 2011, doi: 10.1088/0957-4484/22/46/465602.
- [45] V. Cimrová, S. Eom, V. Pokorná, Y. Kang, and D. Výprachtický, "Hybrid Layers of Donor-Acceptor Copolymers with Homogenous Silver Nanoparticle Coverage for Photonic Applications," *Polymers*, vol. 13, no. 3, p. 439, 2021. [Online]. Available: <https://www.mdpi.com/2073-4360/13/3/439>.
- [46] S. Tougaard, "Quantitative x-ray photoelectron spectroscopy: Simple algorithm to determine the amount of atoms in the outermost few nanometers," *Journal of*

- Vacuum Science & Technology A*, vol. 21, no. 4, pp. 1081-1086, 2003, doi: 10.1116/1.1564040.
- [47] S. Tougaard, "Algorithm for automatic x-ray photoelectron spectroscopy data processing and x-ray photoelectron spectroscopy imaging," *Journal of Vacuum Science & Technology A*, vol. 23, no. 4, pp. 741-745, 2005, doi: 10.1116/1.1864053.
- [48] P. Hu, Y. Cao, D. Jia, and L. Wang, "Selective synthesis of Bi₂Se₃ nanostructures by solvothermal reaction," *Materials Letters*, vol. 64, no. 4, pp. 493-496, 2010/02/28/ 2010, doi: <https://doi.org/10.1016/j.matlet.2009.11.013>.
- [49] T. Uchiyama *et al.*, "Semiconductor–metal transition in Bi₂Se₃ caused by impurity doping," *Scientific Reports*, vol. 13, no. 1, p. 537, 2023/01/11 2023, doi: 10.1038/s41598-023-27701-5.
- [50] M. Li, Z. Wang, L. Yang, X. P. A. Gao, and Z. Zhang, "From linear magnetoresistance to parabolic magnetoresistance in Cu and Cr-doped topological insulator Bi₂Se₃ films," *Journal of Physics and Chemistry of Solids*, vol. 128, pp. 331-336, 2019/05/01/ 2019, doi: <https://doi.org/10.1016/j.jpcs.2017.07.003>.
- [51] L. Xue *et al.*, "First-principles study of native point defects in Bi₂Se₃," *AIP Advances*, vol. 3, no. 5, 2013, doi: 10.1063/1.4804439.
- [52] H. B. Zhang, H. L. Yu, D. H. Bao, S. W. Li, C. X. Wang, and G. W. Yang, "Weak localization bulk state in a topological insulator Bi₂Te₃ film," *Physical Review B*, vol. 86, no. 7, 2012, doi: 10.1103/PhysRevB.86.075102.
- [53] S. Wiedmann *et al.*, "Anisotropic and strong negative magnetoresistance in the three-dimensional topological insulator Bi_2Se_3 ," *Physical Review B*, vol. 94, no. 8, p. 081302, 08/10/ 2016, doi: 10.1103/PhysRevB.94.081302.
- [54] S. Sasmal, J. Mukherjee, D. Suri, and K. V. Raman, "In-depth analysis of anisotropic magnetoconductance in Bi₂Se₃ thin films with electron–electron interaction corrections," *Journal of Physics: Condensed Matter*, vol. 33, no. 46, p. 465601, 2021/09/02 2021, doi: 10.1088/1361-648X/ac1de0.
- [55] R. Sultana, G. Gurjar, S. Patnaik, and V. P. S. Awana, "Growth, Characterization and High-Field Magneto-Conductivity of Co_{0.1}Bi₂Se₃ Topological Insulator," *Journal of Superconductivity and Novel Magnetism*, vol. 32, no. 4, pp. 769-777, 2019, doi: 10.1007/s10948-019-5006-7.
- [56] H. Tang, D. Liang, R. L. J. Qiu, and X. P. A. Gao, "Two-Dimensional Transport-Induced Linear Magneto-Resistance in Topological Insulator Bi₂Se₃ Nanoribbons," *ACS Nano*, vol. 5, no. 9, pp. 7510-7516, 2011/09/27 2011, doi: 10.1021/nn2024607.
- [57] G. Xu *et al.*, "Weak Antilocalization Effect and Noncentrosymmetric

- Superconductivity in a Topologically Nontrivial Semimetal LuPdBi," *Scientific Reports*, vol. 4, no. 1, p. 5709, 2014/07/21 2014, doi: 10.1038/srep05709.
- [58] Y. Kumar, R. Sultana, P. Sharma, and V. P. S. Awana, "Modeling of magnetoconductivity of bismuth selenide: a topological insulator," *SN Applied Sciences*, vol. 3, no. 4, p. 413, 2021/03/04 2021, doi: 10.1007/s42452-021-04397-8.
- [59] E. Amaladass, D. T R, S. Sharma, C. Sundar, A. Bharathi, and A. Mani, "Magneto-transport behaviour of Bi₂Se₃-xTex: Role of disorder," 10/29 2015.
- [60] M. M. Parish and P. B. Littlewood, "Non-saturating magnetoresistance in heavily disordered semiconductors," (in English), *Nature*, Article vol. 426, no. 6963, pp. 162-165, 2003, doi: 10.1038/nature02073.
- [61] D. L. Mo, W. B. Wang, and Q. Cai, "Influence of Thickness on the Electrical Transport Properties of Exfoliated Bi₂Te₃ Ultrathin Films," *Nanoscale Research Letters*, vol. 11, no. 1, p. 354, 2016/08/02 2016, doi: 10.1186/s11671-016-1566-7.
- [62] A. Nivedan *et al.*, "Magnetic field-dependent resistance crossover and anomalous magnetoresistance in topological insulator Bi₂Te₃," *Journal of Physics: Condensed Matter*, vol. 32, no. 42, p. 425002, 2020/07/23 2020, doi: 10.1088/1361-648X/aba06e.
- [63] K. Shrestha, M. Chou, D. Graf, H. D. Yang, B. Lorenz, and C. W. Chu, "Publisher's Note: Extremely large nonsaturating magnetoresistance and ultrahigh mobility due to topological surface states in the metallic Bi_2Te_3 topological insulator [Phys. Rev. B 95, 195113 (2017)]," *Physical Review B*, vol. 95, no. 23, p. 239901, 06/08/ 2017, doi: 10.1103/PhysRevB.95.239901.
- [64] R. Sultana, G. Gurjar, S. Patnaik, and V. P. S. Awana, "High-Field Magneto-Conductivity Analysis of Bi₂Se₃ Single Crystal," *Journal of Superconductivity and Novel Magnetism*, vol. 31, pp. 3075-3078, 2018.